Title

Measurement of the Casimir Effect in the Cylinder-Sphere Geometry

Permalink

https://escholarship.org/uc/item/8b03q55j

Author

Schafer, Robert H

Publication Date

2020

Peer reviewed|Thesis/dissertation

UNIVERSITY OF CALIFORNIA
RIVERSIDE

Measurement of the Casimir Effect in the Cylinder-Sphere Geometry

A Dissertation submitted in partial satisfaction
of the requirements for the degree of

Doctor of Philosophy

in

Physics

by

Robert Schafer

March 2020

Dissertation Committee:

    Dr. Umar Mohideen, Chairperson
    Dr. Roya Zandi
    Dr. Harry Tom

The Dissertation of Robert Schafer is approved:

_____

_____

_____
Committee Chairperson

University of California, Riverside

Acknowledgments

I am grateful to my advisor, without whose help, I would not have been here.

I also would like to thank my committee members, for their invaluable help in finishing this thesis.

All of my colleagues at UCR have helped me at various points along the way. I would like to particularly acknowledge the help I've received from Jun Xu, Mingyue Liu, Christopher Salvo, Rodrigo Castillo-Garza, Alexandr Banishev, Jef Wagner, and Shaolong Chen.

I've made a lot of friends at UCR, too many to enumerate here, but they have been helpful in navigating graduate school in all of its phases. From helping me pass classes in first year, to listening to my practice talks for my qualifying exam, and putting up with me while I finished everything, they were there every step of the way.

Last, but certainly not the least is my fiancée. She was always lending a helping hand. She kept me on course, and trusted that I would get there. She was constantly available whenever I needed a sounding board, and I literally could not have done this without her.

To Christina, I couldn't have done it without you.

To my parents, for all the support and love.

To my friends, for making graduate school fun.

ABSTRACT OF THE DISSERTATION

Measurement of the Casimir Effect in the Cylinder-Sphere Geometry

by

Robert Schafer

Doctor of Philosophy, Graduate Program in Physics
University of California, Riverside, March 2020
Dr. Umar Mohideen, Chairperson

The Casimir effect originates from the boundary effects on the quantum vacuum. The boundary modifies the allowed modes of zero-point, or virtual, photons. Current studies of the Casimir effect have taken place primarily between simple geometries such as the sphere-plate configuration. More complicated geometries will introduce modifications in the collective charge fluctuation anisotropy. In this work, we examine the Casimir force between a cylinder and a sphere in a UHV environment, examining the effects of the 1-D dimensionality of the cylinders. To reduce the ellipticity of the cylinders involved, we have used a glass optical fiber, coated with Au to provide a conductive surface. Co-location of the sphere and cylinder was achieved using a piezoelectric stage with a capacitive sensor controlled PID loop. To maintain cleanliness of the samples and minimize the effect of surface adsorbates, we utilize Ar ion bombardment and UV cleaning. We examine our results using the Proximity Force Approximation (PFA). The Casimir effect has broad implications for MEMS devices operating in the submicron regime.

Contents

List of Figures

Chapter 1

Introduction to the Casimir Effect

1.1 Underpinnings of the Casimir Effect

The Casimir effect was first theorized by Hendrik Casimir as a force occurring between parallel, perfectly conducting plates [1] due to their presence in the quantum vacuum. The presence of the plates modifies the allowed wavelengths for the zero-point photons present in the vacuum of quantum electrodynamics (QED). It was done first for the case of ideal metal plates which have 100% reflectivity. In Casimir's 1948 paper with Dirk Polder first describing the phenomenon, he added the effect of retarded potentials to the standard van der Waals attraction.

The van der Waals force is a distance-dependent interaction arising from the induced dipole moments in atoms or molecules. Though these atoms or molecules have a net charge of zero, on a deeper level they can interact with the electric fields of zero-point photons. The motions in neighboring atoms and molecules create fluctuating electromagnetic fields that show up as instantaneous dipole moments. These coupled dipole oscillations

lead to the van der Waals force. Fritz London developed the quantum theory of the van der Waals interaction[2].

For larger separations, the non-relativistic description is inadequate due to the non-insignificant contribution of the finite speed of light.

1.2 Casimir Effect and Zero-Point Photons

The classical idea of a vacuum was of a completely empty space, free of all particles. As the understanding of quantum mechanics grew, the concept of a quantum vacuum was developed. In a quantum vacuum, while there are no real particles, virtual particles are constantly popping in and out of existence. A classical vacuum does not allow the creation of energy due to the principle of conservation of total energy. At the quantum level, Heisenberg's energy-time uncertainty principle,

$$\delta E \cdot \delta t \geq \frac{\hbar}{2},\tag{1.1}$$

tells us that the conservation of energy is only maintained over large enough timescales. At short timescales, the vacuum energy cannot be determined to an arbitrary degree of precision. This can manifest itself in the creation and annihilation of virtual particles. The interactions these virtual particles have with real matter have been assumed to be the same as the manner in which real particles interact.

The Casimir effect can be understood to be an effect arising from the addition of boundary conditions to the quantum electrodynamic vacuum. In opposition to the classical vacuum, an empty space with nothing inside it, the QED vacuum is filled with zero-point oscillations. Zero-point oscillations are a purely quantum effect, arising from the non-zero

lowest energy possessed by a quantum harmonic oscillator. This energy can be calculated

as a sum over all frequencies. At the ground state, this energy is

$$E_0 = \sum_i \frac{1}{2}\hbar\omega_i. \tag{1.2}$$

Because there are infinite possible frequencies in the QED vacuum, the zero-point

energy is infinite. By introducing the boundary conditions of infinite, perfectly conducting

parallel plates, this infinite sum can be made finite.

Let us write the potential energy as a difference between the energy at distance a

and the energy at infinity:

$$U(a) = E(a) - E(\infty) \tag{1.3}$$

We can write this energy as a set of integrals over the cartesian dimensions:

$$E = \sum_i \frac{1}{2}\hbar\omega_i = c\hbar \int_0^\infty \int_0^\infty \int_0^\infty \sqrt{k_x^2 + k_y^2 + k_z^2}\, \mathrm{d}n_x \mathrm{d}n_y \mathrm{d}n_z. \tag{1.4}$$

If you imagine a set of parallel plates with sides of length L and a separation

distance of a, set up as in Fig. 1.1, you can set up boundary conditions of

$$k_{x,y}L = n_{x,y}\pi \quad \text{and} \quad k_z a = n_z\pi. \tag{1.5}$$

This can be understood as the metal plates limiting the wavelength of virtual,

zero-point photons between them. Changing the plate separation will similarly affect the

allowed range of wavelengths and energies.

Using polar coordinates such that $\sqrt{k_x^2 + k_y^2} = \kappa^2$, we can write

$$E(\infty) = \hbar c \frac{L^2}{\pi^2} \frac{\pi}{2} \int_0^\infty \int_0^\infty \frac{z}{\pi} \sqrt{(\kappa^2 + k_z^2)}\, \kappa\, \mathrm{d}\kappa \mathrm{d}k_z \tag{1.6}$$

3
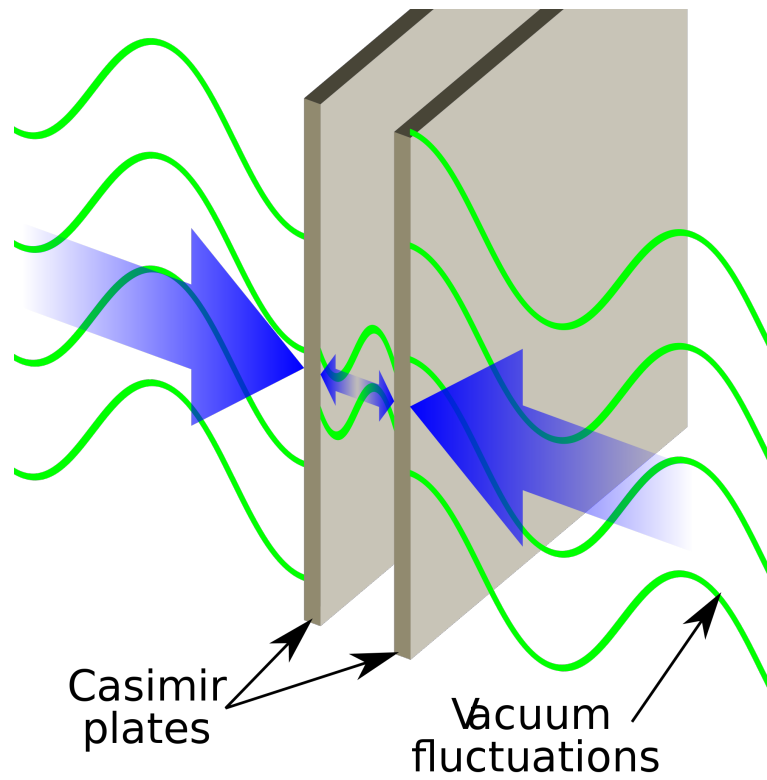
Figure 1.1: The presence of the metal plates modifies the wavelength of the vacuum fluctuations to those which fit in between the plates. (Adapted with permission from Emok (https://commons.wikimedia.org/wiki/File:Casimir plates.svg), Casimir plates, https://creativecommons.org/licenses/by-sa/3.0/legalcode)

and

$$E(a) = \hbar c \frac{L^2}{\pi^2} \frac{\pi}{2} \sum_{(0)1}^{\infty} \int_0^{\infty} \sqrt{\left(\left(\frac{n\pi}{a}\right)^2 + \kappa^2\right)} \kappa \mathrm{d}\kappa. \tag{1.7}$$

In the previous equation, the (0)1 under the sum indicates that the first term in the sum is to be halved. Further, we have made the substitution $k_z = \frac{n\pi}{a}$.

When you use eq. (1.7) and eq. (1.6) in eq. (1.3), the result is divergent. To combat this, Casimir introduced a cut-off function, $f\left(\frac{k}{k_m}\right)$. This function is one for $k << k_m$, but will quickly go to zero as $\frac{k}{k_m} \to \infty$. Here, k_m is assumed to be on the order of the plasma frequency of the metals comprising the plates, $k_m \approx \frac{\omega_p}{c}$. Effectively, this means that high-frequency waves are transparent and not bounded by the plates.

We can now make the substitution $u = \frac{a^2 \kappa^2}{\pi^2}$ and obtain

$$U(a) = \frac{\pi^2 \hbar c L^2}{4a^3} \left[\sum_{(0)1}^{\infty} \int_0^{\infty} \sqrt{n^2 + u} f\left(\frac{\pi\sqrt{n^2 + u}}{ak_m}\right) \mathrm{d}u \right. \\ \left. - \int_0^{\infty} \int_0^{\infty} \sqrt{n^2 + u} f\left(\frac{\pi\sqrt{n^2 + u}}{ak_m}\right) \mathrm{d}u \mathrm{d}n \right]. \tag{1.8}$$

We can now apply the Euler-Maclaurin formula:

$$\sum F(n) - \int F(n) \mathrm{d}n = -\frac{1}{12} F'(0) + \frac{1}{720} F'''(0) \tag{1.9}$$

where

$$F(n) = \int_{n^2}^{\infty} \sqrt{\omega} f\left(\frac{\omega\pi}{ak_m}\right) \mathrm{d}\omega. \tag{1.10}$$

Here we have made the substitution $\omega = u + n^2$ and adjusted the integration limits appropriately.

The derivative of $F(n)$ is

$$F'(n) = -2n^2 f\left(\frac{n^2\pi}{ak_m}\right), \tag{1.11}$$

giving us the Euler Maclaurin terms:

$$F'(0) = 0 \tag{1.12}$$

and

$$F'''(0) = -4. \tag{1.13}$$

All of the other terms go quickly to zero as κ approaches zero. The Casimir energy is

$$U(z) = -\left(\frac{\pi^2 \hbar c}{720 z^3}\right) L^2. \tag{1.14}$$

To find the Casimir pressure, we take the derivative $-\frac{\partial U}{\partial z}$ and divide by the area of the plates, L^2. We obtain

$$P_{cas}(z) = \frac{\pi^2 \hbar c}{240 z^4}. \tag{1.15}$$

This equation depends only on the reduced Planck's constant, $\hbar$, the speed of light, c, and the distance between the plates, z. This is interesting because it implies that the Casimir effect is both a quantum effect (through the inclusion of $\hbar$), and a relativistic effect (through c).

1.3   Relativistic van der Waals force

The van der Waals force is a well known force that occurs between closely spaced neutral atoms. Even though the atoms have no net charge, they will interact with the electric field of the zero-point photons. The fields from these dipoles will cause other atoms

6

to become polarized and there will be a resulting dipole-dipole attractive force between the atoms. The electric field due to a dipole at a distance r away is

$$\mathbf{E_0} = \frac{3(\mathbf{p_0} \cdot \hat{\mathbf{d}})\hat{\mathbf{d}} - \mathbf{p_0}}{d^3}.$$

(1.16)

The interaction energy between the two dipoles will then go as r^{-6}. In Casimir's original paper, he and Polder considered the effect of relativistic retardation when the distance between dipoles increases to the point where the retardation is non-negligible. Due to the finite speed of the interaction particles of the electric field, there is a correction to the short-separation van der Waals force. The interaction energy becomes [3]

$$U_{int} = -\frac{23}{4\pi}\hbar c \frac{\alpha_1 \alpha_2}{r^7}.$$

(1.17)

Here, α_1 and α_2 are the static polarizabilities of the atoms, and the energy now goes as r^{-7}.

The connection between the van der Waals force and the Casimir force was later expanded upon by E.M. Lifshitz in 1956. He started from Maxwell's equations to create a generalized description of the effect which would reduce to the limiting cases of ideal boundaries automatically[4]. He also studied how the fluctuations would behave in the presence of real metals, not the assumed, ideal metals. We will go further into this expansion in Chapter 2 of this thesis.

1.4 Casimir Effect Applications

Due to the intersection of quantum and relativistic effects inherent in the Casimir effect, it can provide insight into a multitude of different sub-fields of physics, among them: condensed matter, particle physics, cosmology, and atomic and molecular physics. The

dominance of the Casimir effect at short ranges over standard electromagnetic effects also leads to engineering implications as the feature size for technology continues to move into the nanoscale realm.

1.4.1 Applications in Fundamental Physics

The Casimir effect can be used as a vehicle for studying many different topics in condensed matter physics. Previous studies have looked into thin films[5], critical systems[6], varying boundary conditions[7, 8, 9], especially those with different geometries[10, 11], surface tension[12], and cryophysics[13]. Material properties and carrier concentrations have also been shown to have a role in the Casimir effect.

In the field of atomic and molecular physics, the Casimir effect is used to probe atom-atom and atom-wall interactions, and is useful in studying the subject of cavity quantum electrodynamics[14, 15].

In cosmology, the boundary effects on vacuum polarization are important for some string theories, as well as for understanding the value of the cosmological constant[16, 17].

For particle physics, Casimir force measurements can further constrain Yukawa-type interactions in nucleon physics, constraining the presence of new particles that extend the field beyond the Standard Model[18, 19, 20, 21, 22]. This has gained further importance after the collapse of most supersymmetric extensions to the Standard Model in the wake of the most current LHC measurements.

1.4.2   Applications in Micro and Nano-scale Engineering

With micro-machine feature sizes shrinking further and further, the Casimir effect is becoming important in characterizing and controlling the balance of forces at that scale. At a distance of about 10 nm, the Casimir pressure will be as large as 1 atmosphere. This is a large enough force that it needs to be taken into account. One proposed transistor architecture that purports to reduce the problem of leakage current and waste power dissipation is the use of micro or nano electromechanical switches[23]. The modulation of these switches and the modeling of their function can be achieved through judicious use of the Casimir effect. The traditional Casimir effect is an attractive force, which can lead to unwanted behavior if not anticipated[24, 25, 26]. It may be possible to switch the sign of the Casimir effect using a combination of material choice, non-standard geometric assemblies, or modification of charge carrier density through the use of incident light[10, 27, 28]. Modeling of nanoscale moving parts also requires consideration of the effects from the Casimir force[29, 30].

1.5   Historical Overview of Casimir Force Measurements

After Casimir first proposed the existence of the Casimir effect, it only took a decade for someone to attempt a measurement of the effect. Marcus Sparnaay, in 1958, set up a spring-balance system with metal plates[31]. He aimed for separation distances between 500 nm and 2μm. Using capacitive sensing to detect the separation of the plates, he was able to achieve a distance resolution of 10 nm, with a force sensitivity of 1-10 nanonewtons. There were a number of issues with this experimental set-up. To achieve a

minimal residual potential difference, the plates were touched together at the start of the experiment. This still left a small V_0, which would not be compensated for by applying a compensatory voltage. There was no attempt to eliminate the existence of a metal-oxide layer. The plates used were very rough at the scale of the separation distance, leading to a large uncertainty in the absolute separation distance. The two plates were made parallel just by sight, which introduced more error in the separation distance. Though this first experiment had too much experimental error to directly compare the results to theory, it strongly indicated the existence of the force.

The next important experiment was published by Bloklan and Overbeek in 1978[32]. The measurement was done using a spring balance measuring the force between a lens and a flat plate coated with varying depths of chromium. To reduce the effect of surface charges, the surfaces were exposed to water vapor. Their experiment aimed to minimize the effect of the potential difference between the surfaces through application of external voltages and measuring the residual potential difference. The separation distance was measured using the capacitance in the lens-plate system. Chromium proved difficult to model theoretically due to strong absorption bands in the spectrum. The authors estimated their accuracy to be roughly 50%. This experiment was most important due to the experimental design setting out and attempting to reduce the important systematic errors that still need to be dealt with in modern experiments.

A more modern attempt was performed by S.K. Lamoreaux in 1997[33]. His force measurement device was a torsional pendulum instead of the spring balance system used by Sparnaay. To avoid the parallelization issues cause by the plate-plate geometry, Lamoreaux

used a spherical lens and a plate, both coated with Cu and then Au. This experiment was additionally performed in a low vacuum, of about .1 mTorr. This experiment claimed agreement between its experimental results and the theoretical values at the level of 5% but the agreement was obtained by subtracting a hypothetical electrostatic force of unknown origin.

A year later, Umar Mohideen and Anushree Roy used an atomic force microscope to take measurements of the Casimir effect between 100 and 900 nm. They reported a deviation between their results and the theory of 1%[8].

Further measurements have proceeded using similar experimental set-ups. Many have used a frequency shift technique, using an oscillating cantilever in a modified AFM setup[34, 35]. Others have continued using micromechanical torsion oscillators[7] and some have used commercially available accelerometers to measure the Casimir force[36].

1.6   Overview of Thesis

We have already discussed a basic level understanding of the idealized Casimir force and its relationship to the van der Waals effect. Additionally, we have gone over some potential applications for the Casimir effect, both in fundamental physics and applications. We have also briefly covered selected historical experiments leading up to the current state of the field.

In Chapter 2, we will go in depth regarding the Lifshitz theory of the Casimir effect in real metals, with a focus on the role of dissipation in metals. Chapter 3 will discuss the set-up of our measurements, going over the physical components that are essential to our

work. Next, Chapter 4 will cover the procedures and calibrations used in the data collection and analysis. Chapter 5 will discuss our results and the conclusions drawn. We will follow this with our conclusions and proposals for future work.

Chapter 2

Lifshitz Theory

In 1956, Lifshitz generalized the dispersion forces in an attempt to unify the van der Waals force and the Casimir effect[4]. The initial formulation by Casimir had assumed ideal metals. Lifshitz's theory allowed for real materials. In this chapter, we will present calculations for the Lifshitz theory at both zero temperature and non-zero temperature. We will also discuss differing theoretical models regarding the role energy dissipation plays in the behavior of zero-point photon scattering from real materials.

2.1   Parallel Plate Dielectrics at T = 0

Let us start by considering the case of identical, parallel, dielectric regions, separated by a gap of width a. This is illustrated in figure 2.1.
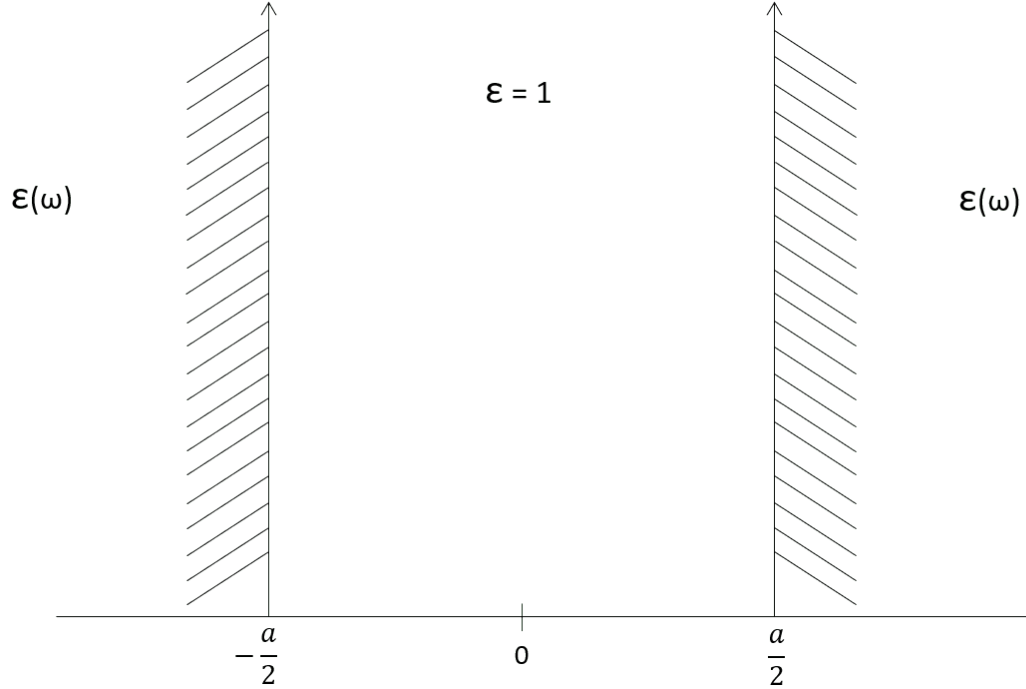
Figure 2.1: Depicted are two dielectric semispaces, set up with a gap of width a between them. The permittivities within the semispaces are given by $\epsilon(\omega)$S

We can express the permittivity in this example as

$$
\varepsilon(\omega, \boldsymbol{r}) =
\begin{cases}
\varepsilon(\omega), & \text{for } |z| \geq a/2, \\[2mm]
1, & \text{for } |z| < a/2.
\end{cases}
\tag{2.1}
$$

The electromagnetic basis of the forces we are considering leads us to start with Maxwell's core electromagnetic equations. Here, they are presented assuming zero charge or current flow.

$$
\begin{aligned}
&\boldsymbol{\nabla} \cdot \boldsymbol{D}(t, \boldsymbol{r}) = 0, && \boldsymbol{\nabla} \times \boldsymbol{E}(t, \boldsymbol{r}) + \frac{1}{c}\frac{\partial \boldsymbol{B}(t, \boldsymbol{r})}{\partial t} = 0, \\[3mm]
&\boldsymbol{\nabla} \times \boldsymbol{B}(t, \boldsymbol{r}) - \frac{1}{c}\frac{\partial \boldsymbol{D}(t, \boldsymbol{r})}{\partial t} = 0, && \boldsymbol{\nabla} \cdot \boldsymbol{B}(t, \boldsymbol{r}) = 0,
\end{aligned}
\tag{2.2}
$$

where $\boldsymbol{D}$ is the electric displacement, $\boldsymbol{E}$ is the electric field, and $\boldsymbol{B}$ is the magnetic induction.

14

To set up proper boundary conditions, we need the continuity boundary conditions to hold at the boundary:

$$E_{Lt}(t, \boldsymbol{r}) = E_{Rt}(t, \boldsymbol{r}), \qquad D_{Ln}(t, \boldsymbol{r}) = D_{Rn}(t, \boldsymbol{r}),$$
$$B_{Ln}(t, \boldsymbol{r}) = B_{Rn}(t, \boldsymbol{r}), \qquad B_{Lt}(t, \boldsymbol{r}) = B_{Rt}(t, \boldsymbol{r}). \tag{2.3}$$

Here, the subscript n and t indicates that the direction of the vector is normal to the boundary and tangential to the boundary plane respectively.

The displacement is related to the electric field by:

$$\boldsymbol{D}(\omega, \boldsymbol{r}) = \varepsilon(\omega, \boldsymbol{r}) \boldsymbol{E}(\omega, \boldsymbol{r}) \tag{2.4}$$

and

$$\boldsymbol{D}(t, \boldsymbol{r}) = \int_{-\infty}^{t} \varepsilon(t - t', \boldsymbol{r}) \boldsymbol{E}(t', \boldsymbol{r}) dt'. \tag{2.5}$$

We will start by assuming the existing electric and magnetic fields are of a single frequency ω,

$$\boldsymbol{E}(t, \boldsymbol{r}) = \boldsymbol{E}(\boldsymbol{r}) e^{-i\omega t}, \qquad \boldsymbol{B}(t, \boldsymbol{r}) = \boldsymbol{B}(\boldsymbol{r}) e^{-i\omega t}. \tag{2.6}$$

By using equations (2.4) and (2.6), Maxwell's equations (eq. (2.2)) can be written as:

$$\boldsymbol{\nabla} \cdot \boldsymbol{E}(\boldsymbol{r}) = 0, \qquad \boldsymbol{\nabla} \times \boldsymbol{E}(\boldsymbol{r}) - i\frac{\omega}{c} \boldsymbol{B}(\boldsymbol{r}) = 0,$$
$$\boldsymbol{\nabla} \times \boldsymbol{B}(\boldsymbol{r}) + i\varepsilon(\omega)\frac{\omega}{c} \boldsymbol{E}(\boldsymbol{r}) = 0, \qquad \boldsymbol{\nabla} \cdot \boldsymbol{B}(\boldsymbol{r}) = 0. \tag{2.7}$$

We can use these to find the wave equations for electric and magnetic fields:

$$\boldsymbol{\nabla}^2 \boldsymbol{E}(\boldsymbol{r}) + \varepsilon(\omega)\frac{\omega^2}{c^2} \boldsymbol{E}(\boldsymbol{r}) = 0,$$
$$\boldsymbol{\nabla}^2 \boldsymbol{B}(\boldsymbol{r}) + \varepsilon(\omega)\frac{\omega^2}{c^2} \boldsymbol{B}(\boldsymbol{r}) = 0, \tag{2.8}$$

which have eq. (2.6) as a solution.

We can now describe the energy that exists in the EM field between the two dielectrics in terms of the force carrier eigenfrequencies in the transverse electric and magnetic (TE and TM) modes:

$$U(a) = \frac{\hbar}{4\pi} \int_0^\infty k_\perp dk_\perp \sum_n^\infty \left(\omega_{k_\perp,n}^{\mathrm{TE}} + \omega_{k_\perp,n}^{\mathrm{TM}} \right) A. \tag{2.9}$$

In this equation, $k_\perp$ refers to the gaussian average of the wave numbers in the x and y directions. $\omega_{k_\perp,n}^{\mathrm{TM,TE}}$ are the photon eigenfrequencies, and A is the area of interaction. This should bring to mind the equation for the energy of harmonic oscillators in a vacuum, eq. (1.2).

We will now follow a process similar to our derivation in the first chapter. This energy is infinite, so in order to find a value that is finite and meaningful, we will need to look at a difference of energies. The meaningful distances we are choosing for our gap size are a and ∞.

$$
\begin{aligned}
E(a) &= \frac{U(d=a)}{A} - \frac{U(d=\infty)}{A} \\[2em]
&= \frac{\hbar}{4\pi^2} \int_0^\infty k_\perp dk_\perp \int_0^\infty d\xi \Big\{ \ln \left[1 - r_{\mathrm{TE}}^2(i\xi, k_\perp) e^{-2qa} \right] \\[2em]
&\quad + \ln \left[1 - r_{\mathrm{TM}}^2(i\xi, k_\perp) e^{-2qa} \right] \Big\}.
\end{aligned}
\tag{2.10}
$$

Here we have used the replacements $\xi = -i\omega$, the imaginary frequency, $q^2 = q^2(i\xi, k_\perp) = k_\perp^2 + \frac{\xi^2}{c^2}$, $k^2 = k^2(i\xi, k_\perp) = k_\perp^2 + \varepsilon(i\xi)\frac{\xi^2}{c^2}$.

The Fresnel reflection coefficients, $r_{\mathrm{TE}}(i\xi, k_\perp)$ and $r_{\mathrm{TM}}(i\xi, k_\perp)$ are given by:

$$r_{\mathrm{TE}}(i\xi, k_\perp) = \frac{\varepsilon(i\xi)q(i\xi, k_\perp) - k(i\xi, k_\perp)}{\varepsilon(i\xi)q(i\xi, k_\perp) + k(i\xi, k_\perp)}, \tag{2.11}$$

16

and

$$r_{\text{TM}}(i\xi, k_\perp) = \frac{q(i\xi, k_\perp) - k(i\xi, k_\perp)}{q(i\xi, k_\perp) + k(i\xi, k_\perp)}. \tag{2.12}$$

Now, we can find the Casimir pressure by taking the derivative of eq. (1.3).

$$P_{Cas}(a) = -\frac{\hbar}{2\pi^2} \int_0^\infty \int_0^\infty k_\perp dk_\perp d\xi q \Big\{ \big[r_{\text{TE}}^{-2}(i\xi, k_\perp) e^{2qa} - 1 \big]^{-1} + \big[r_{\text{TM}}^{-2}(i\xi, k_\perp) e^{2qa} - 1 \big]^{-1} \Big\}. \tag{2.13}$$

We can examine this equation at the limit where the distance between the dielectrics is much smaller than the characteristic absorption wavelength of the material. At this limit, we find the pressure to be:

$$P(a) = -\frac{H}{6\pi a^3}, \tag{2.14}$$

where H is the Hamaker constant, given by:

$$H = \frac{3\hbar}{8\pi} \int_0^\infty d\xi \int_0^\infty y^2 dy \Bigg\{ \bigg[\frac{\varepsilon(i\xi) + 1}{\varepsilon(i\xi) - 1} \bigg]^2 e^y - 1 \Bigg\}^{-1} \tag{2.15}$$

and $y = 2aq$[37].

As we expected, the limit of small separation returns a result equal to the non-retarded van der Waals pressure.

When we look at the other limit, where the separation distance is much larger than the characteristic wavelength, we find the pressure to be

$$P(a) = -\frac{\pi^2 \hbar c}{240 a^4}, \tag{2.16}$$

when we look at the case of an ideal metal. This pressure is, as we expect, what we found with eq. (1.15).

2.2 Dielectrics at Non-zero Temperatures

So far, our calculations have only looked at the fluctuations arising from quantum effects. When we generalize to non-zero temperatures, thermal fluctuations also will play a role in the Casimir effect[38, 39]. We will study this case using the same geometry as in the zero temperature calculations.

To start with, we will now write the permittivity of the materials as

$$\varepsilon(\omega) = 1 + \sum_{j=1}^{K} \frac{g_i}{\omega_j^2 - \omega^2 - i\gamma_j\omega},$$
(2.17)

where ω_j is the oscillator frequencies of the electrons, g_i are the oscillator strengths, γ_j are the damping parameters, and K is the number of oscillators.

Instead of the energy, we will consider the free energy of the system, due to the non-zero temperature. This free energy is given by

$$\mathcal{F} = -k_{\mathrm{B}}Tln\mathcal{Z}.$$
(2.18)

Here, k_{B} is the Boltzmann constant and $\mathcal{Z}$ is the Gibbs partition function, given by

$$\mathcal{Z} = \sum_{n} e^{-E_n/k_{\mathrm{B}}T}.$$
(2.19)

The free energy of the system, given eq. (2.17) is

$$\mathcal{F}(a,T) = \frac{k_{\mathrm{B}}T}{2\pi} \sum_{(\mathbb{Z})}^{\infty} \int_0^{\infty} k_{\perp}dk_{\perp} \left\{ \ln\left[1 - r_{\mathrm{TE}}^2\left(i\xi_l, k_{\perp}\right)e^{-2aq_l}\right] + \ln\left[1 - r_{\mathrm{TM}}^2\left(i\xi_l, k_{\perp}\right)e^{-2aq_l}\right] \right\},$$
(2.20)

where $(\mathbb{Z})$ means the set of all integers, with the 0 term halved. ξ_l are the discrete Matsubara frequencies, given by

$$\xi_l = 2\pi\frac{k_{\mathrm{B}}T}{\hbar}l.$$
(2.21)

18

We can now find the Casimir pressure at non-zero temperature is

$$P(a,T) = -\frac{k_{\mathrm{B}}T}{\pi} \sum_{(\mathbb{Z})}^{\infty} \int_0^{\infty} q_l k_{\perp} dk_{\perp} \left\{ \left[r_{\mathrm{TE}}^{-2}(i\xi,k_{\perp}) e^{2aq_l} - 1 \right]^{-1} + \left[r_{\mathrm{TM}}^{-2}(i\xi,k_{\perp}) e^{2aq_l} - 1 \right]^{-1} \right\}.$$

(2.22)

The Matsubara frequencies' reflection coefficients are:

$$r_{\mathrm{TE}}(i\xi_l, k_{\perp}) = \frac{\varepsilon_l q_l - k_l}{\varepsilon_l q_l + k_l}, \qquad r_{\mathrm{TM}}(i\xi_l, k_{\perp}) = \frac{q_l - k_l}{q_l + k_l}, \tag{2.23}$$

with

$$q_l^2 = k_{\perp}^2 + \frac{\xi_l^2}{c^2}, \quad k_l^2 = k_{\perp}^2 + \varepsilon_l \frac{\xi_l^2}{c^2}, \quad \varepsilon_l = \varepsilon(i\xi_l). \tag{2.24}$$

2.3 Casimir Force Between Real Metals

So far, we have only included the effects of forces acting upon core electrons. In metals, rather than dielectrics, conduction electrons begin to play a large role in the conductivity and characterization of metals. At low frequencies, we can approximate this using the free electron model, writing the electric field wave equation as

$$\nabla^2 \boldsymbol{E} + \frac{\omega^2}{c^2}(1 - \frac{\omega_{\mathrm{p}}^2}{\omega^2})\boldsymbol{E} = 0. \tag{2.25}$$

Here, an important parameter to keep in mind is ω_{p}, the plasma frequency. This is effectively the frequency at which the electron density will oscillate naturally, given the Coulomb restoring force. It is given by

$$\omega_{\mathrm{p}} = \sqrt{\frac{4\pi n_e e^2}{m^*}}, \tag{2.26}$$

where n_e is the number density of the conduction electrons, e is the elementary charge, and m^* is the effective mass of the electrons.

There are two models with which we can proceed. We need to consider the behavior of zero-point photons when they scatter from real conduction electrons. For real electromagnetic waves, the interaction causes some dissipation of energy. This leads to a permittivity given by

$$\varepsilon_{\mathrm{D}}(\omega) = 1 - \frac{\omega_{\mathrm{p}}^2}{\omega(\omega + i\gamma)},$$ (2.27)

where γ is the relaxation constant, equal to $\omega_{\mathrm{p}}/4\pi\sigma_0$. σ_0 is the static conductivity of the metal. This model is well known as the Drude model, based on the 1900 work of Paul Drude[40]. However, this theory leads to some issues, resulting in the violation of the third law of thermodynamics, the Nernst heat theorem[41, 42, 43]. According to the third law, as a system approaches absolute zero, the entropy should reach a minimum value. For a perfect crystal lattice, this value should be equal to 0. But the relaxation term in the Drude model will lead to a non-zero value for the Casimir entropy.

Another approach is the plasma model, where it is assumed that no dissipation of energy takes place between the virtual particles and the conduction electrons. For the plasma model, the permittivity is

$$\varepsilon_{\mathrm{p}}(\omega) = 1 - \frac{\omega_{\mathrm{p}}^2}{\omega^2}.$$ (2.28)

which is easily seen by setting the relaxation parameter, γ, to zero. The plasma model can be found to be consistent with the laws of thermodynamics, but is not adequate in explaining the behavior of real particle interactions.

2.4 Correction for Finite Conductivity

So far we have considered dielectrics and ideal metals, but we need to correct for the effect of non-infinite conductivity when we are dealing with real metal surfaces. For a finite conductivity, we have a non-zero skin depth. We can expand the Lifshitz equation, eq.(2.10) over powers of δ_0/a[41], resulting in

$$E_{\rm p}(a) = -\frac{\pi^2 \hbar c}{720 a^3}\left[1 - 4\frac{\delta_0}{a} + \frac{72}{5}\left(\frac{\delta_0}{a}\right)^2 - \frac{320}{7}\left(1 - \frac{\pi^2}{210}\right)\left(\frac{\delta_0}{a}\right)^3 + \frac{400}{3}\left(1 - \frac{163\pi^2}{7350}\right)\left(\frac{\delta_0}{a}\right)^4\right],$$

$$(2.29)$$

where the skin depth is related to the plasma wavelength, $\lambda_{\rm p}$ by

$$\delta_0 = \frac{\lambda_{\rm p}}{2\pi}. \tag{2.30}$$

This leads us to a Casimir pressure, including finite conductivity corrections, of

$$P_{\rm p}(a) = -\frac{\pi^2 \hbar c}{240 a^4}\left[1 - \frac{16}{3}\frac{\delta_0}{a} + 24\left(\frac{\delta_0}{a}\right)^2 - \frac{640}{7}\left(1 - \frac{\pi^2}{210}\right)\left(\frac{\delta_0}{a}\right)^3 + \frac{2800}{9}\left(1 - \frac{163\pi^2}{7350}\right)\left(\frac{\delta_0}{a}\right)^4\right].$$

$$(2.31)$$

For large separations, or small skin depths, these equations will approach the Casimir energy and pressure that we have previously calculated for ideal metals, eq.(1.14) and eq.(1.15).

2.5 Proximity Force Approximation in the Sphere-Cylinder Geometry

The geometry of the boundaries involved in the production of the Casimir force will have a large effect on the modifications of the zero-point photon spectrum. Previous studies

have looked at different geometries. Tuning the force based on the involved geometries is a unique and interesting control parameter. Early work seems to indicate that we need to go beyond a basic extrapolation from the parallel planes.

Many studies have used a sphere-plane geometry, due to the difficulty of parallelization inherent in the two plane system. One approach for approximating the Casimir and electromagnetic forces is to use a proximity force approximation (PFA). In this section, we will examine the PFA for a sphere-cylinder geometry.

To begin with, we define a proximity energy as the sum over the areas of the parallel plate separation with some corrections[44]. With a small gap curvature, only the parallel sections of the interacting surfaces need to be considered. The contributions of the perpendicular surfaces become negligible.

We will consider a gap width between the surfaces as

$$D(x, y) = z + \frac{1}{2}D_{xx}x^2 + \frac{1}{2}D_{yy}y^2 + higher\ orders \tag{2.32}$$

D_{xx} and D_{yy} are the second derivatives of the gap width with respect to x and y.

Now we can write the proximity energy in terms of this gap width. We can write

$$U_{prox}(z) = 2(R_x R_y)^{1/2} \int \int d\xi d\nu E_{pp}(D), \tag{2.33}$$

where we have made the substitutions $\xi = x/(2R_x)^{1/2}$ and $\nu = y/(2R_y)^{1/2}$ so that we can write D as $D = z + \rho^2$ where $\rho^2 = \xi^2 + \nu^2$. The next step is to transform our integrals into one integral over ρ,

$$U_{prox}(z) = 2(R_x R_y)^{1/2} \int_0^\infty 2\pi\rho d\rho E_{pp}(D). \tag{2.34}$$

This becomes

$$U_{prox}(z) = 2\pi \bar{R} \int_{D=z}^{\infty} dD E_{pp}(D), \tag{2.35}$$

or

$$U_{prox}(z) = 2\pi \bar{R} E_{pp}(z). \tag{2.36}$$

In this equation, $\bar{R}$ is the effective Gaussian curvature between the two surfaces. For a sphere-plate geometry, it is simply the radius of curvature of the sphere involved. Due to the combination of curvatures present in the cylinder-sphere geometry, we need to account for the cylinder radius as well. This $\bar{R}$ is given by [45]

$$\bar{R}_{sc} = R_s \left(1 + \frac{R_s}{R_c}\right)^{-1/2}. \tag{2.37}$$

This provides a starting point for the consideration of the effect of geometry on the Casimir effect. In our experiment, the radii chosen are large when compared to the separation distance.

Chapter 3

Experimental Set-up

In this chapter, we will discuss the apparatus. For reference, a schema for the experiment is shown in fig. 3.1.

3.1 Vacuum Systems

We chose to do our experiments in a high vacuum environment for a number of reasons; the most important of which is achieving the purity and homogeneity of the interacting Au surfaces. Impurities, adsorbates, and contaminants change the material properties. When using the frequency shift technique, any air will serve to dampen the oscillations of the cantilever, reducing the sensitivity of our results. Argon ion and UV cleaning were done in vacuum in order to allay this.

Our vacuum chamber was made of a six-way stainless steel cross, with 8" CF flanges that pressed a knife-edge into a copper gasket in order to create an airtight seal. Apertures to pumps were controlled by gate valves to maintain a pressure as low as 10^{-9}
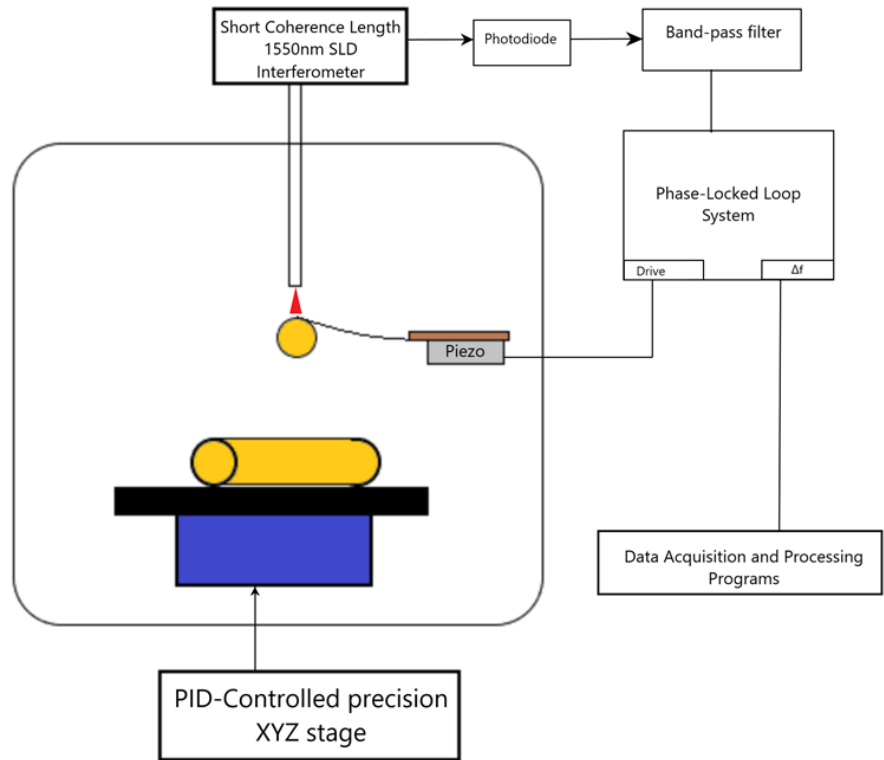
Figure 3.1: This figure shows a schematic diagram of the components in the experiment. The laser interferometer, cantilever with attached sphere, gold coated cylinder, positioner, and electronics are depicted.

torr and section off pumps while not in use. The chamber is placed on a damped optical table in order to reduce the effect of external vibrations.

3.1.1 Pumps and Gauges

The vacuum was achieved through a multi-stage pumping system. The first pump was a roughing pump, to bring the initial pressure down to 10^{-3} torr. We used a Varian SH-110 oil-free scroll pump. This pump was chosen to reduce the contamination of the chamber by vacuum pump oils. It was switched on first, and the pressure of the chamber

reduced over the course of a few minutes. The vacuum pressure at this stage was measured using a Pirani gauge.

The scroll pump was connected to the chamber through a turbomolecular pump. This pump was a Varian TV-301. It lowered the pressure through momentum transfer. The pump was essentially a rapidly spinning turbine that would impart a net momentum in the direction of the scroll pump through collisions with the gas molecules. Over the course of about 10 minutes, it would get up to its operating rotation speed and bring the pressure of the chamber down further. Given enough time, this pump would bring the chamber to about 10^{-8} torr. Pressures in this range were measured with an ionization gauge.

One disadvantage of the scroll and turbomolecular pumps is that they vibrated when active. This is an added source of mechanical noise that would make measurements in the system difficult. To combat this, once the pressure had been reduced sufficiently, an ion diode pump was switched on. This pump would ionize remaining gas in the chamber and drive the gas molecules to be captured in the pump, reducing the pressure further. This pump would achieve stable pressures of 10^{-9} torr in our set-up.

3.1.2 Feedthroughs

In order to gain electrical access as well as send laser light into the chamber, we used a variety of feedthroughs. Most of the feedthroughs were standard ceramic coaxial feedthroughs. These controlled the grounding and voltage control of the cantilever and plate as well as the driving of the piezoelectric block that moved the cantilever. Further electrical feedthroughs, in the form of serial ports, were used to control the x, y, and z movement of the n-point sample stage.

We also had an optical feedthrough that was manufactured for this experiment. A small hole was drilled into a blank CF 1.25" flange and an optical fiber was fed through that hole. The hole was then sealed with high-vacuum appropriate epoxy, namely Torr-seal, in order to seal the hole. The fiber jacket and coating were removed around the site of the epoxy application to remove the possibilities of leaks through the layers of the fiber coating or jacket. The design of this feedthrough negates the power loss associated with fiber bulkhead connectors.

3.1.3   External Positioning

The positioning of the cantilever relative to the sample surface was very important. Previous studies have mostly utilized the sphere-plate geometry or geometries that are not sensitive to planar positions. The only positioning necessary was the surface separation between the sphere and cylinder. We were forced to position micron-scale geometries relative to each other with nanoscale precision. This was achieved through a coarse and a fine positioner.

Coarse Positioner

The coarse positioner was a three axis micrometer system. The micrometers are operated manually from outside of the vacuum chamber. The z-axis can move 4 inches, the x and y axes are restricted to half an inch of travel. They are laser etched with micrometer scales for repeatability of positioning. The vacuum is maintained through a welded bellows tube, with CF copper gasket connections.

Fine Positioner

There is also a fine positioner located within the chamber. It is a 3 axis piezoelectric stage manufactured by nPoint. The x and y axes will move over a 100 micron range, while z is limited to 25 microns. The positioning is measured and controlled by a capacitive sensor feeding into a PID loop to maintain position. The closed loop position noise according to the manufacturer is 3 angstroms in x and y, and 1 angstrom in z. There are settling times of 8 ms in x and y, and 3 ms in z.

3.2 Interferometry

In order to measure the frequency of oscillation of the cantilever, we use a short coherence fiber optic interferometer.

3.2.1 Interferometric Principles

The interferometer works by detecting the interference of light. Due to the wave behavior of light, coherent light will interfere with light of the same wavelength depending on the phase difference. Our set-up uses a cleaved optical fiber positioned over the cantilever. Some of the light will reflect off of the cleaved end of the fiber, while the rest will be transmitted through and proceed to reflect off the top side of the cantilever, as shown in fig.3.2. Both reflection signals will travel back through the fiber, to be detected by the photodiode. The distance between the fiber end and the cantilever will induce a phase difference in the signals. When the path length difference is an even multiple of $\lambda/2$, the light will interfere destructively. When it is an odd multiple, the light interferes constructively.
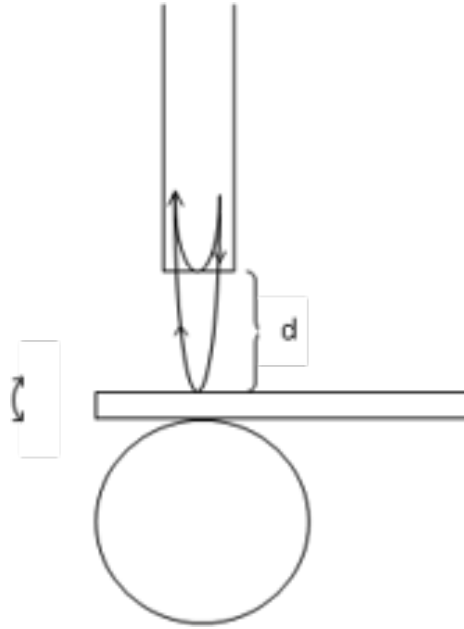
Figure 3.2: The interferometric cavity is shown here. Some light is reflected from the cleaved end of the fiber, and the rest is transmitted through. This transmitted light will reflect off the top side of the cantilever, and go back into the fiber with an added path difference of $2d$. The light will interfere based on the added path difference relative to the wavelength.

3.2.2 Interferometer Light Source

The light source we are using is a fiber coupled super luminescent diode (SLD) with a wavelength of 1550 nm. The power and temperature are both controlled, and the output power was held at 1.2 mW. The temperature of the laser was stabilized using an insulated enclosure constructed from 2 inch thick styrofoam. The temperature stability as measured by a thermocouple was $\pm$ .1 Celsius over the course of a day. The SLD had a coherence length of 66 μm. This short coherence length was chosen in order to reduce the effect of stray reflections and other interferences on the signal.

3.2.3   Interferometer Fibers and Alignment

The laser is connected initially through a FC/APC connection to a 2x2 fused fiber optic 50/50 directional coupler, shown in fig. 3.3. This coupler has a return loss of -55 dB. The laser is fed into input 1, and is then split into fibers 3 and 4. Fiber 3 is connected through an FC/APC connector to the chamber fiber. Fiber 2 received the reflected signal and transmit it to the photodiode. The signal in fiber 4 is unused and is terminated in an index-matching liquid to avoid any reflections off of its end.
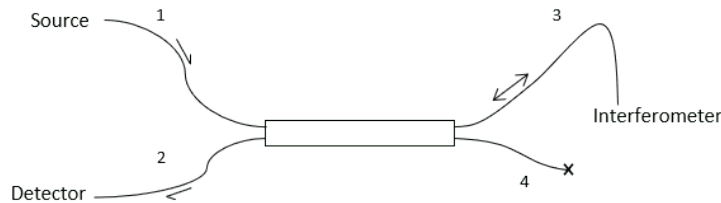
Figure 3.3: The fiber coupler is shown here. The light initially comes from the source, is split passing through the coupler, then the reflected light will pass back through the coupler and be detected by the photodiode.

For the fiber inside of the chamber, we used a single mode optical fiber with an operating wavelength range of 1310 to 1550 nm. The fiber is made of germanium doped silica, and has a diameter of 125 microns. The fiber is fed into the chamber through a feedthrough and connected externally to the 2x2 fiber coupler. The bare fiber is held in place by a friction chuck mounted to the positioning arm.

To align the fiber end with the cantilever, the cantilever assembly is mounted on a 3 axis manual micropositioner system. The active core diameter for the fiber we used was 5 microns, and our cantilevers are roughly 35 microns wide, so there was a range of positions which would give us reflections. Some portions of the top of the cantilever will have a

stronger reflectivity, due to coating imperfections and surface adsorbates. The alignment is checked by monitoring the power level of the returning laser signal. A larger signal indicates a strong reflection from the cantilever. We maximized the signal power during the alignment.

All of our fibers are fixed in position in order to prevent low frequency vibrations from contributing to the interferometric signal. The fiber we use has a low bending and splice loss to further reduce the low-frequency noise.

3.2.4   Photodiode Detector

We used a 900-1700 nm, low noise, InGaAs detector to detect the changes in the light signal from the interferometer. It was connected through a fiber optic FC/APC connector, and was responsible for transforming the light signals into electrical signals. The detector has variable output gain, and is adjusted to the optimal value prior to a data run. The output was through a standard co-axial cable.

3.3   Piezoelectrics

The cantilever oscillation and quarter-point positioning is carried out through the use of a lead zirconate titanate (PZT) piezoelectric ceramic block.

3.3.1   Cantilever Holder

The cantilever is mounted on a copper tongue through the use of conductive epoxy, to ensure good electrical connection for grounding. An oxide layer is removed before at-

tachment. This copper tongue is mounted on a ceramic holder suitable for use in ultra high-vacuum. The holder has electrical connections for use with the piezoelectric voltage application and for the grounding of the cantilever. Sections of the holder facing the measurement region are coated with a conductive layer to prevent stray electric fields and charge accumulation from affecting the experiment. In other regions, the same effect is achieved through layers of gold coated aluminum foil placed over surfaces.

3.4   Cleaning

The Casimir force measurement can be adversely affected by the presence of residual electrostatic forces due to patch potentials on the sphere and cylinder surfaces. These patch potentials would provide an additional attractive electrostatic force[46, 47, 48, 49].

Patch potentials can be caused by a few things. One source is that the crystalline domains on a surface will not be of the same crystallographic orientation, leading to patches of different domains, each with a different work function. For gold, which coats both interaction areas of our sphere and cylinder, the three possible surface crystallite orientations are $\langle 100 \rangle$, $\langle 110 \rangle$, and $\langle 111 \rangle$. These orientations will have work functions of 5.47 eV, 5.37 eV, and 5.31 eV respectively[50, 51]. The contribution from these domains should be negligible as long as the domain size is small.

Another possible source is surface adsorbates on top of the gold layer. These adsorbates can lead to work function inhomogeneity on the surfaces and can contribute significantly to a patch potential effect. To combat this, we used *in situ* cleaning through UV radiation and argon ion cleaning.

3.4.1 UV Cleaning

The primary mechanism of action for UV cleaning is photosensitized oxidation[52, 53]. The UV radiation first will excite the bonds of the contaminant molecules. This will cause some to be removed. Diatomic oxygen is split into atomic oxygen and ozone is produced. The atomic oxygen will oxidize the contaminant hydrocarbons on the surface. The sample surface is cleaned of patches, but the chamber itself is also cleaned, leading to a better vacuum.

3.4.2 Argon Ion Cleaning

For argon ion cleaning, argon is leaked into the chamber at a pressure of about 10^{-5} torr, ionized through electron impact, and then accelerated towards the sample through an accelerating voltage of 500 V. The ions bombard the surface and remove the surface adsorbates through physical momentum transfer. The bombardment is targeted, cleaning only the surfaces the argon stream is pointed towards. Secondary impacts will spread this cleaning out, but the argon ion cleaning is not sufficient to clean the whole chamber.

3.5 Cantilever

We used a specialized AFM cantilever for this experiment. It was tipless, unlike traditional AFM cantilevers. The cantilever was made from machined silicon, and was conductive. The conductivity is necessary in creating an electrical connection to the sphere for grounding it.

3.5.1 Cantilever Fabrication

The spring constant of the cantilever was reduced through HF and KOH etching. This reduced the thickness of the cantilever, reducing the spring constant according to the equation

$$k = \frac{Y * width * thickness^3}{4 * length^4}, \tag{3.1}$$

where Y is the Young's modulus. The reduction in spring constant is meant to decrease the noise.

After the etching, the sphere was attached to the cantilever tip. The spheres were made from hollow glass, chosen for being smooth and having a low eccentricity. The glass spheres were prepared through the process described in refs [34] and [54]. A large sphere was chosen and picked up electrostatically with a stripped optical fiber. It was placed on the end of the cantilever where a small conductive epoxy was pre-applied.

After attachment, gold was evaporated onto the sphere by using an electron-beam evaporator. After coating the bottom of the sphere, the holder was flipped over and angled to coat the top of the cantilever and ensure an overlap of the conductive surface. The gold was layered at a rate of 2 angstroms per second until the thickness was 100 nanometers. The bulk of the cantilever was masked during the coating process. This served to limit the increase in mass and thickness, keeping the spring constant low.

After force measurements were taken, the sphere was removed from the system and placed in a scanning electron microscope (SEM) for accurate measurement of the radius. After taking the images, a program called ImageJ was used to analyze them in order to find the radius. After picking a point on the edge of the sphere, a line was drawn to the

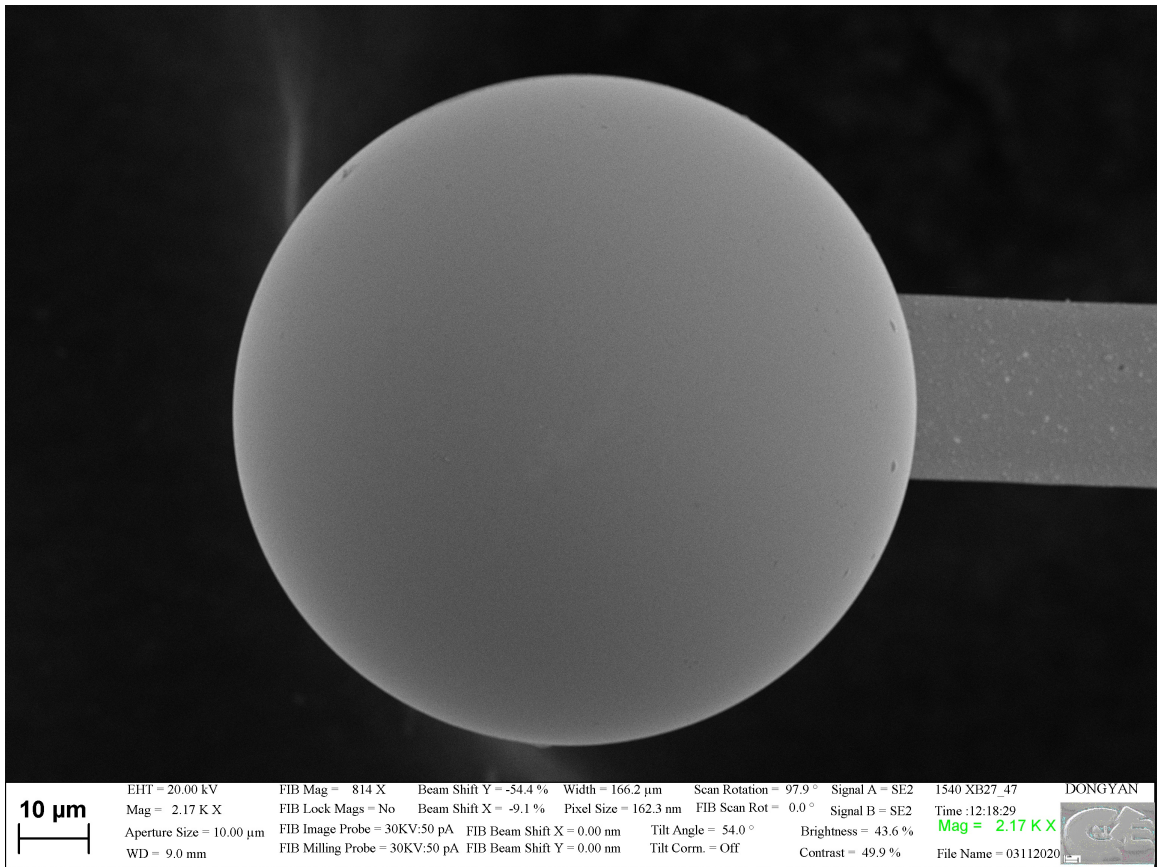|						
10 μm	EHT = 20.00 kV	FIB Mag = 814 X	Beam Shift Y = -54.4 %	Width = 166.2 μm	Scan Rotation = 97.9 °	Signal A = SE2	1540 XB27_47	DONGYAN
	Mag = 2.17 K X	FIB Lock Mags = No	Beam Shift X = -9.1 %	Pixel Size = 162.3 nm	FIB Scan Rot = 0.0 °	Signal B = SE2	Time :12:18:29
	Aperture Size = 10.00 μm	FIB Image Probe = 30KV:50 pA	FIB Beam Shift X = 0.00 nm	Tilt Angle = 54.0 °	Brightness = 43.6 %	Mag = 2.17 K X
	WD = 9.0 mm	FIB Milling Probe = 30KV:50 pA	FIB Beam Shift Y = 0.00 nm	Tilt Corrn. = Off	Contrast = 49.9 %	File Name = 03112020

Figure 3.4: Scanning electron microscope picture of the sphere on the tip of the cantilever. The radius was measured to be $47.65 \pm .0605$ microns.

point on the circumference of the sphere that was furthest away, measuring the diameter. This was repeated four times, picking diameters such that the angle between consecutive lines was 45 degrees. This process was then repeated on another image of the same sphere, taken at a 90 degree angle in the SEM, in order to reduce any systematic effects caused by the aspect ratio of the scan. The results of the analysis showed a diameter of 95.3 microns. The error in this measurement has three sources. The systematic error is chiefly from the aspect ratio distortion, and it was found to be 103 nm. The resolution error was found by looking at the pixel size of the image, and was 47 nm. The repeated measurements also showed a random error that was 42 nm. The total error in this measurement was therefore 121 nm. The radius is then $47.65 \pm .0605$ microns.

3.6 Sample Surface and Cylinders

The cylindrical surface we chose needed to have a radius under 100 microns and have low eccentricity. Many options were considered, from wires to micro-machined metal rods. The best option was optical fiber. The optical fiber is widely commercially available and fits the stated requirements. The fiber we ended up using was an 80 micron diameter silica fiber. The optical properties are not important, only the physical dimensions. The deviation of the optical fiber from the shape of a perfect cylinder was well below 1 micron.

3.6.1 Fabrication

The fiber was attached to a smooth silicon wafer using conductive epoxy. Both ends of the fiber were coated in the conductive epoxy. Care was taken to ensure that the

fiber was flat against the wafer surface. After curing, the assembly was coated with 100nm of gold in an electron-beam evaporator. After the coating process, an electrical lead was attached using conductive epoxy.

After force measurements were taken, the diameter of the cylinder was measured in a similar manner to the method described for the sphere measurements. We found the cylinder diameter to be 80.2 microns, with random errors of 48 nm, and resolution error of 47 nm. The aspect ratio distortion was not measured specifically for the cylinder, but is taken to be equal to that in the sphere measurement, 103 nm, due to the measurements taking place in the same SEM system. The radius of the cylinder was $40.1 \pm .062$ microns.

3.6.2 Motivation for Use of Cylinders

As discussed earlier, the collective interactions of the fluctuations in charge density and current due to zero-point and thermal photon oscillations are one approach towards explaining the source of the Casimir effect. With a cylinder, you effectively transition the length scale of the geometry to a 1-D dimensionality. This causes a strong anisotropy in the charge fluctuations. When examined through the dissipationless approach, the Casimir pressure between two cylinders will display material independent behavior at large separation distances, in contrast to the Drude model, which includes the effect of dissipation and transitions into material dependent behavior at large separations. This behavior is unexpected, especially in light of the material independence the Drude approach has at intermediate separations[55].
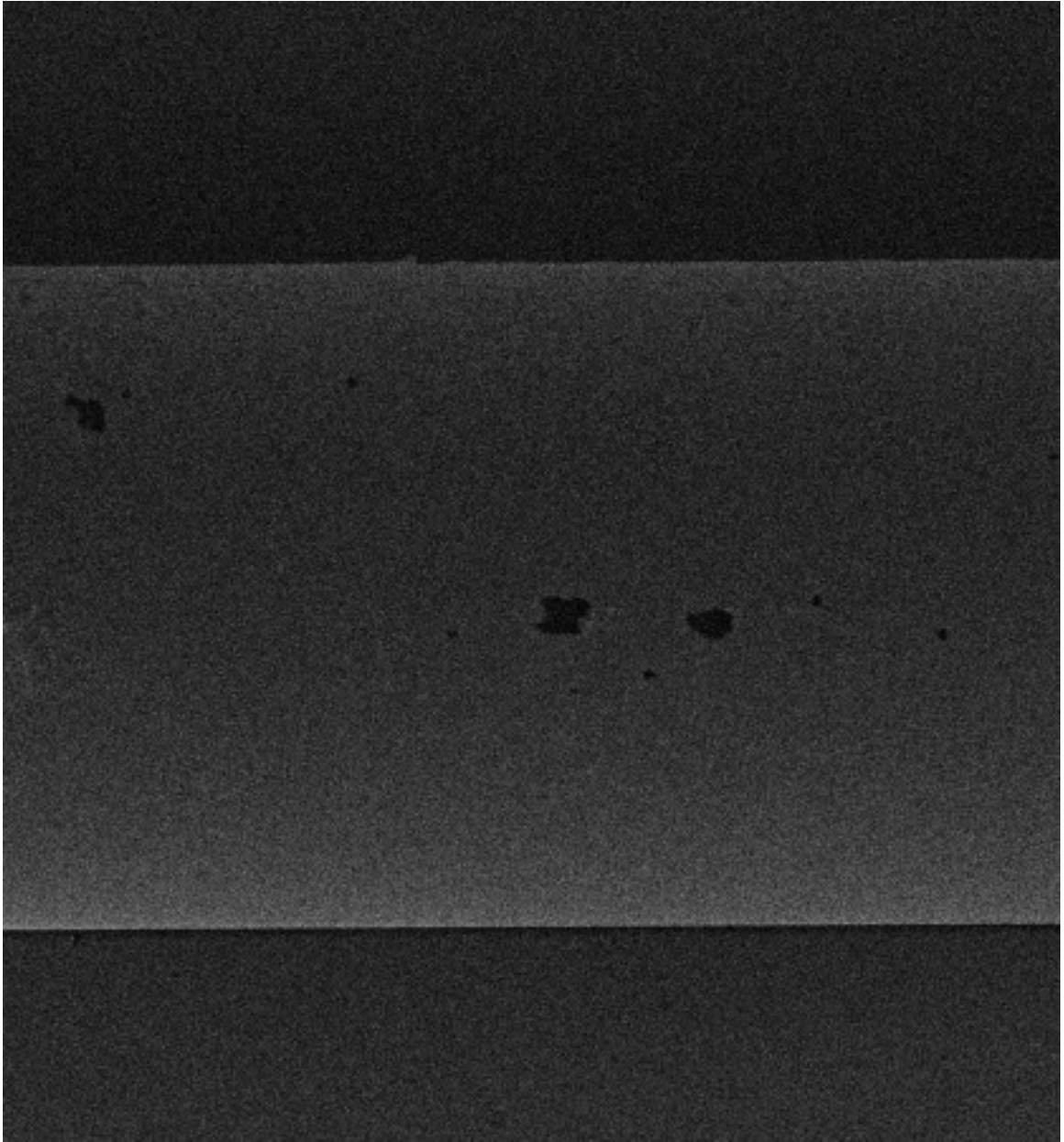
Figure 3.5: Scanning electron microscope image of the cylinder. The radius of the cylinder was $40.1 \pm .062$ microns.

Chapter 4

Experimental Procedures

4.1 Frequency Shift Technique

In order to detect the force acting on the cantilever, we opted to use a dynamic frequency shift technique instead of measuring the static deflection due to the higher force detection sensitivity. In this method, the cantilever is treated as a damped harmonic oscillator. The equation of motion for a damped harmonic oscillator being acted upon by an external force is

$$m\frac{d^2z}{dt^2} + \frac{m\omega_0}{Q}\frac{dz}{dt} + k(z - z_0) = F_{\text{ext}}(z). \tag{4.1}$$

where ω_0 is the angular frequency of the undamped oscillator at infinite sphere-cylinder separation, k is the spring constant, equal to $m\omega_0^2$, and $F_{\text{ext}}(z)$ is the external force acting on the oscillator.

Figure 4.1: An illustration of the frequency shift that a cantilever undergoes when subjected to an external force.
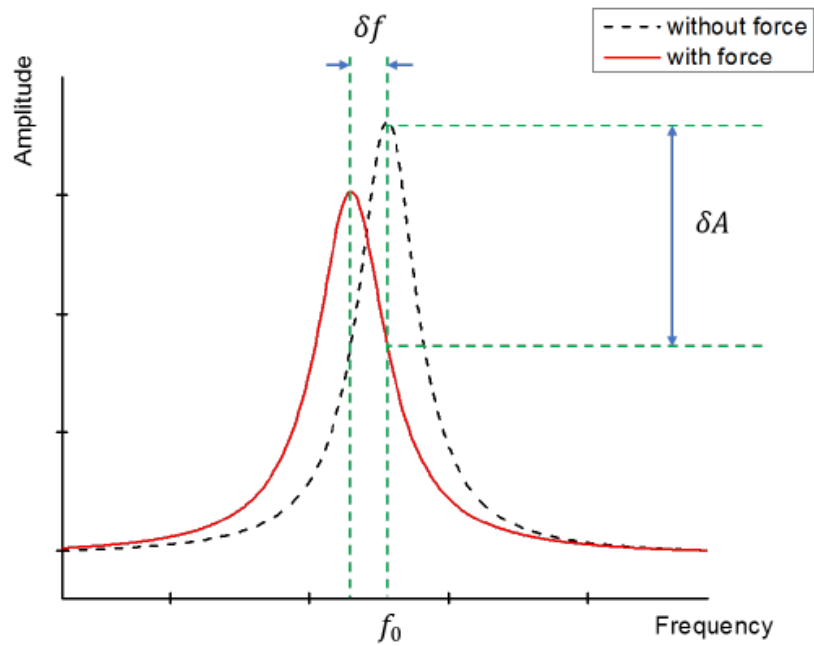
We can assume a small amplitude and Taylor expand this external force around the rest position, z_0 to first order.

$$F_{\text{ext}}(z) = F_{\text{ext}}(z_0) + (z - z_0)\left(\frac{\partial F_{\text{ext}}}{\partial z}\right)_{z=z_0} \tag{4.2}$$

We can substitute eq. (4.2) into eq. (4.1) and get

$$m\frac{d^2 z}{dt^2} + \frac{m\omega_0}{Q}\frac{dz}{dt} + \left(k - \left(\frac{\partial F_{\text{ext}}}{\partial z}\right)_{z=z_0}\right)(z - z_0) = F_{\text{ext}}(z_0). \tag{4.3}$$

This shows that the resonance frequency of the cantilever will shift from ω_0 to

$$\omega_{new} = \omega_0\sqrt{1 - \frac{1}{k}\left(\frac{\partial F_{\text{ext}}}{\partial z}\right)}. \tag{4.4}$$

If the gradient of the external force, evaluated at z is much smaller than the spring constant, we can write the frequency shift as

$$\Delta\omega = \omega - \omega_0 = -\frac{\omega_0}{2k}\left(\frac{\partial F_{\text{ext}}}{\partial z}\right)_{z=z_0}. \tag{4.5}$$

If we assume that the driving force is sinusoidal, this becomes:

$$m\frac{d^2 z}{dt^2} + \frac{m\omega_0}{Q}\frac{dz}{dt} + k(z - z') = F_0\sin(\omega t), \tag{4.6}$$

where the driving force is F_0 and the driving frequency is ω. This is a second order differential equation, with the solution

$$z(t) = z' + A(f)\sin(\omega t + \phi). \tag{4.7}$$

In the solution, $A(f)$ is the oscillation amplitude, equal to

$$A(f) = \frac{F_0/m\omega_0^2}{\sqrt{(1 - (\omega/\omega_0))^2 + (\omega/(\omega_0 Q))^2}}, \tag{4.8}$$
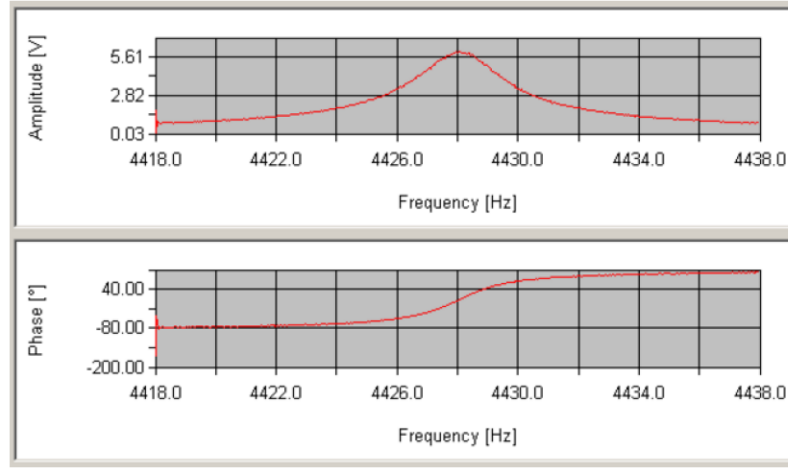
41

Figure 4.2: The process of finding the phase shift in the PLL software. The program will sweep its output frequency and measure the phase difference. The point with the highest amplitude is the resonant frequency and there should be a clear inflection point for the phase shift at the corresponding point. This value is the phase shift setting we use.

and the phase of the oscillation with respect to the driving force is given by

$$\phi = \arctan\left(\frac{\omega\omega_0}{(\omega^2 - \omega_0^2)Q}\right) + n\pi. \tag{4.9}$$

In order to measure the resonant frequency and adjust the driving frequency, we use a phase-locked loop (PLL) control system. The controller will measure the input frequency and phase and will output a driving signal to the piezo driving the cantilever that is held at a constant phase difference with respect to the input frequency. The result is an output frequency that is constantly changing to stay at the same frequency as the input frequency through maintaining the phase difference.

The actual PLL device we use has a frequency lock range of ±183 Hz with a 5 mHz resolution for the frequency shift. We've set the bandwidth to be 50 Hz. The optimum

settings for the phase shift are determined though maximization of the oscillation amplitude.

The frequency shift is due to an external force that is a combination of the electrostatic and Casimir forces acting on the cantilever. To isolate the effect of the Casimir force, we can split up the external force.

$$
\begin{aligned}
F_{ext} &= F_{ele} + F_{Cas} \\
&= \gamma(V - V_0)^2 + F_{Cas}
\end{aligned}
$$
(4.10)

The electrostatic force will go as some factor (γ) multiplied by the potential difference between the applied voltage and the residual voltage.

We can plug eq. (4.10) into (4.5) and get

$$
\Delta\omega = -\frac{\omega_0}{2k}\frac{\partial F_{ext}}{\partial z} = -\frac{\omega_0}{2k}\left(\frac{\partial\gamma}{\partial z}\right)(V - V_0)^2 - C\frac{\partial F_{Cas}}{\partial z},
$$
(4.11)

where

$$
C = \frac{\omega_0}{2k}.
$$
(4.12)

Rearranging, we obtain:

$$
\frac{\partial F_{cas}}{\partial z} = -\frac{1}{C}[\Delta\omega - \beta(V - V_0)^2]
$$
(4.13)

4.2 Alignment

A key factor in measuring the force between the sphere and the cylinder is positioning the center of the sphere directly over the axis of the cylinder. Deviations from this position can induce lateral forces that we have not accounted for. Smaller deviations will increase the minimum distance between the points of closest approach and limit the range of separations we are able to study.

The alignment process starts by roughly aligning the sphere and cylinder optically using a red laser sent through the fiber interferometer positioned over the sphere. Then, a large voltage is applied between the sphere and cylinder in order to increase the electrostatic force acting on the cantilever. This will cause a correspondingly large deflection, as shown by eq. 4.11.

The frequency shift is monitored while the position is swept through the x and y axes. The electrostatic force will be at a maximum when the separation distance is minimized. The coarse positioner is used first, and the position at which the frequency shift is maximized is noted using the micrometer markings on the positioner. After the coarse positioning, the x-y piezoelectric positioner inside the vacuum chamber is used. The x-y position is once again swept until the maximum frequency shift is observed. This position corresponds to the alignment of the sphere center and cylinder axis.

Once this position is set, it is maintained over the timescales needed for a measurement. We found a difference in positioning of only 2 microns over the course of 3 hours. The positioning was checked and reset before every data run.

4.3   Data Acquisition Procedure

To find the Casimir force as a function of distance, we will move the plate relative to the cantilever while monitoring the frequency shift. Voltages are applied between the cylinder and sphere to subtract out the electrostatic contribution.

Starting at maximum separation, the cylinder was moved upwards in 5 nm steps. At each step, two data points were taken, measuring the applied voltage, frequency shift,
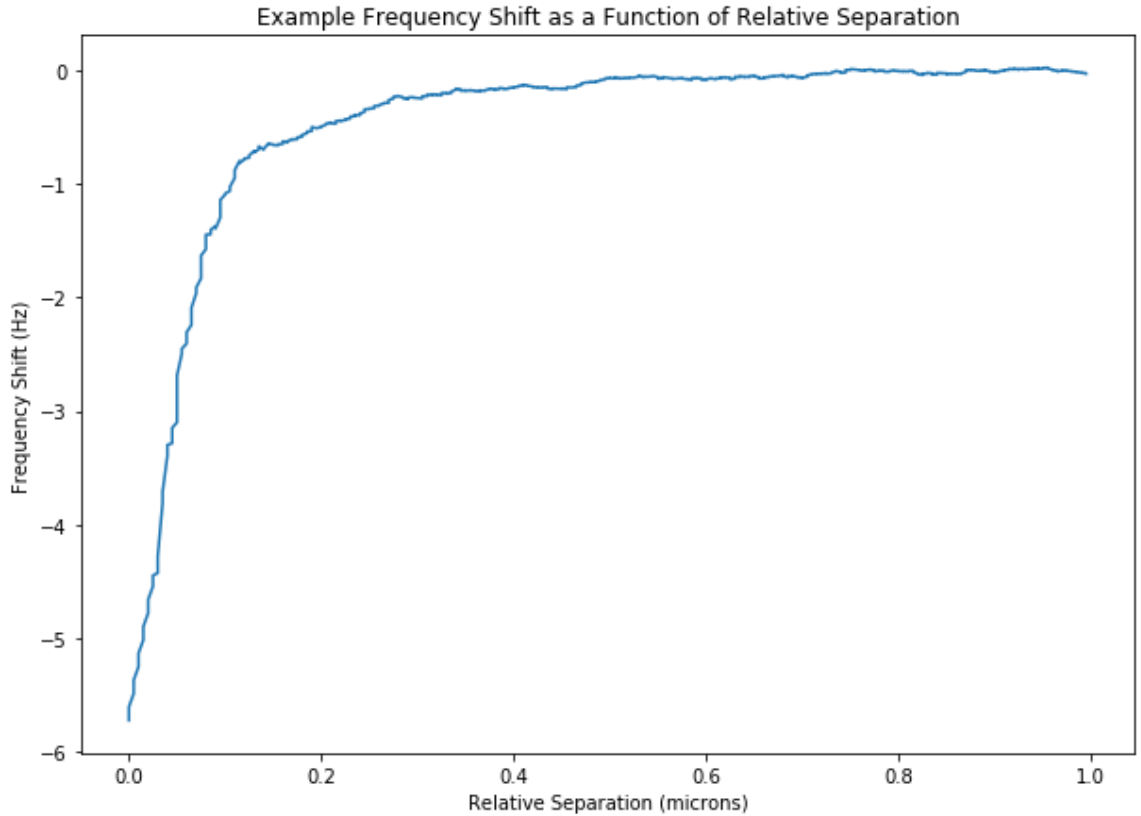
Figure 4.3: The frequency shift as a function of distance for a sample run. As the relative distance is reduced, the force acting on the cantilever increases, leading to a negative frequency shift.

plate location, and time. The plate was moved over a total distance of one micron each time. This procedure was repeated 11 times, with a different voltage applied between the sphere and cylinder each time. The sphere was held at ground, while the voltage was applied to the plate. Voltages were chosen in steps of 15 mV above and below the measured residual potential, with 5 above and 5 below.

4.3.1 Drift Correction

The final 10 shifts were all done at the residual potential voltage. This was done to calculate a drift correction for the interaction distance. If the drift was non-existent, these 10 runs would be identical. By examining the distances at which these runs would reach a certain deflection, and comparing them with the timestamps, we are able to find the rate of the drift between the sphere and cylinder, and then compensate for it.

An additional ten sets of frequency shift versus separation data were taken, with the applied potential voltage being set equal to the residual potential. These repeated measurements would return identical sets of data if there was no drift in the system, due to the external force acting on the cantilever being the same in each case. Examination of the data set shows that the same frequency shift signal occurs at different separations. By comparing the separations at one frequency shift signal with the timestamps associated with their measurements, we are able to calculated the drift rate.

This process is done by choosing a frequency shift signal $\Delta\omega$, comparing the separations at which each individual run achieves that shift, and plotting the separations versus the time elapsed. This plot of the separations versus the time is shown in fig. 4.4. The points are fit with a linear regression to get the drift rate.

The average drift rate for the runs included in this thesis was .875 angstroms per second. This corresponds to about 5.25 nm in one minute, or about 125 nanometers over the course of the measurement.
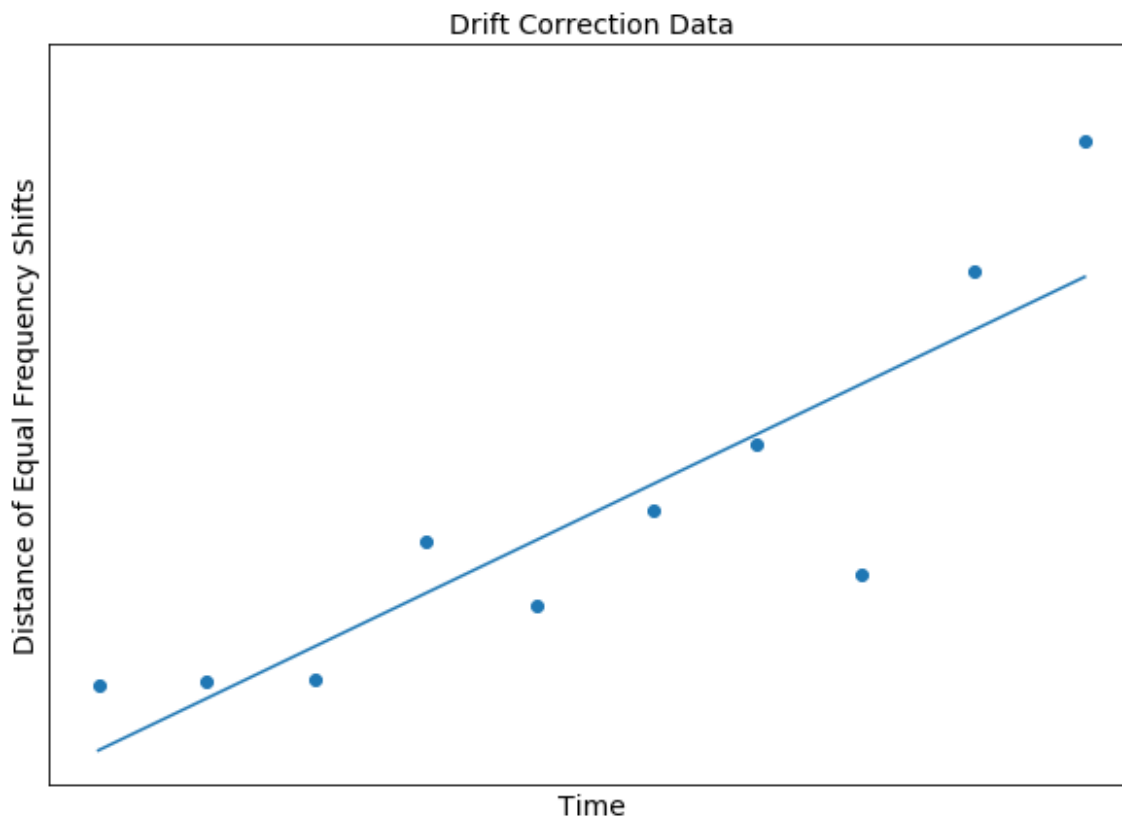
Figure 4.4: An example of the drift correction data is shown here. The dots are the individual measurements and the line is a linear fit of the drift. The time is reported during the data measurement using UNIX time, and the distances were measured by looking for the reported relative separation at which the frequency shift of the drift correction runs reaches a specified value. This is averaged for each run over a series of frequency shift targets to obtain the distances. The average drift rate in this experiment was .875 angstroms per second.

4.4 Electrostatic Compensation

The force acting on the cantilever is comprised of the electrostatic force as well as the Casimir force. The characterization of the electrostatic force is important for the elimination of the effects and the isolation of the Casimir force. To understand the form of the electrostatic force, we will begin by examining it through the use of the proximity force approximation.

To start with the proximity force approximation, remembering eq. (2.36), we can write the electrostatic force as a function of the plate-plate energy:

$$F_{ele} = 2\pi \bar{R} E_{pp} \tag{4.14}$$

The $\bar{R}$ is the Gaussian curvature between the two surfaces, given by

$$\bar{R} = R_s \left(1 + \frac{R_s}{R_c}\right)^{-\frac{1}{2}}. \tag{4.15}$$

The plate-plate electrostatic energy is given by

$$E_{pp} = \frac{1}{2}\frac{C}{A}(V + V_0)^2 = \frac{1}{2}\frac{\varepsilon_0}{z}(V - V_0)^2 = \frac{\varepsilon_0}{2z}(V - V_0)^2. \tag{4.16}$$

Thus, the electrostatic force is

$$F_{ele} = \frac{\pi \varepsilon_0}{z_r + z'} R_s \left(1 + \frac{R_s}{R_c}\right)^{-\frac{1}{2}} (V - V_0)^2 \tag{4.17}$$

and the gradient of the electrostatic force becomes

$$\frac{\partial F_{ele}}{\partial z} = -\frac{\pi \varepsilon_0}{z^2} R_s \left(1 + \frac{R_s}{R_c}\right)^{-\frac{1}{2}} (V - V_0)^2. \tag{4.18}$$

For simplicity's sake, we will write this in the form of $\beta(V_{app} - V_0)^2$, with β given by

$$\begin{aligned} \beta &= \frac{\omega_0}{2k}\frac{\pi \varepsilon_0}{z^2} R_s \left(1 + \frac{R_s}{R_c}\right)^{-\frac{1}{2}} \\ &= \frac{\omega_0}{2k}\frac{\pi \varepsilon_0}{(z_r + z')^2} R_s \left(1 + \frac{R_s}{R_c}\right)^{-\frac{1}{2}}. \end{aligned} \tag{4.19}$$
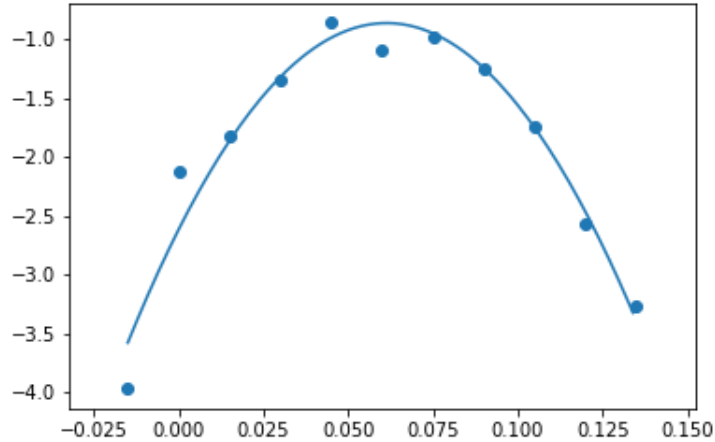
48

Figure 4.5: An example of the parabolas produced by taking points from each run, at equal separation distances, and plotting the frequency shift measured at that distance against the voltage applied for that run. The resulting points are plotted against the parabola equation (eq. $\Delta\omega = \beta(V - V_0)^2 + gradCas$) and the resulting fit is plotted on top of the points.

The effects of the electrostatic force gradient on the frequency shift are parabolic in nature. When the applied voltage, V_{app}, is equal to the residual potential, V_0, the electrostatic force will be zero. At this point, the only frequency shift remaining is due to the effect of the Casimir force. We can see this in fig. 4.5. Through finding the parabolae and their curvature and vertex coordinates, we are able to subtract out the electrostatic force. The subtraction of the electrostatic force will isolate the effects of the Casimir force.

4.4.1   Computation of Electrostatic Force Using a Numerical Technique

The electrostatic proximity force approximation was checked against a computational simulation of the electromagnetic force between the sphere and cylinder. The program used was COMSOL, and it worked using the finite element method for solving for the electric potential, from which the force can be calculated using the Maxwell Stress Tensor. To

begin with, the geometry and materials were defined. We created a sphere and cylinder, with their centers aligned along the z-axis. The cylinder radius was set at 40 microns and the sphere radius at 50 microns to represent the size of the objects used in the physical experiment. The separation distance was parameterized and varied to study the effect the separation distance would have on the force. A large bounding sphere was set with a radius of 1.2 cm. The material constants were set as elemental gold, from the built-in library.

The next step was to solve the governing equation with the given boundary conditions. The relevant governing equation for electrostatic effects is the Poisson equation, $\nabla^2 \varphi = -\frac{\rho}{\varepsilon}$. We set the boundary conditions such that charge is conserved everywhere, and the sphere and the bounding, large sphere were grounded. The surface of the cylinder was set at a potential of 1 Volt.

The numerical simulation works by solving for the electric field and potential at each point in a three dimensional grid. The grid size was determined by the physics engine, with a minimum element size of 200 nm, and a maximum element size of 20 microns. The growth rate of the elements was limited to 1.3.

The force was calculated over a variety of distances, and compared with the PFA results. An agreement of .1% was found between the numerical simulations and the PFA calculated data.

4.5 Determination of Absolute Distance

Fitting the parabolas to the equation $\Delta \omega = \beta(V - V_0)^2 + gradCas$, we are able to obtain a value for β, the parabola curvature. From this, we can compare the dependence of

the β value with respect to distance with the β we found with eq. (4.19), fitting the data to the theory to obtain a value for the absolute distance, z'. The fitting process used was a least-squares fit. The fitting procedure was repeated with increasingly small subsets of the β vs. distance plot.

Chapter 5

Experimental Results and

Comparison with Theory

5.1   Residual Potential Voltage

The data we processed has a residual potential that is, on average, -61.4±4.1 mV. This represents the potential that needs to be applied to minimize the electrostatic force between the sphere and the cylinder. A graph of the residual potential as a function of distance is seen in fig. 5.1.The graph is noisy, but broadly flat. The variance increases at larger distances due to the fact that the frequency shift curve is flatter at these distances, leading to a smaller signal-to-noise ratio.
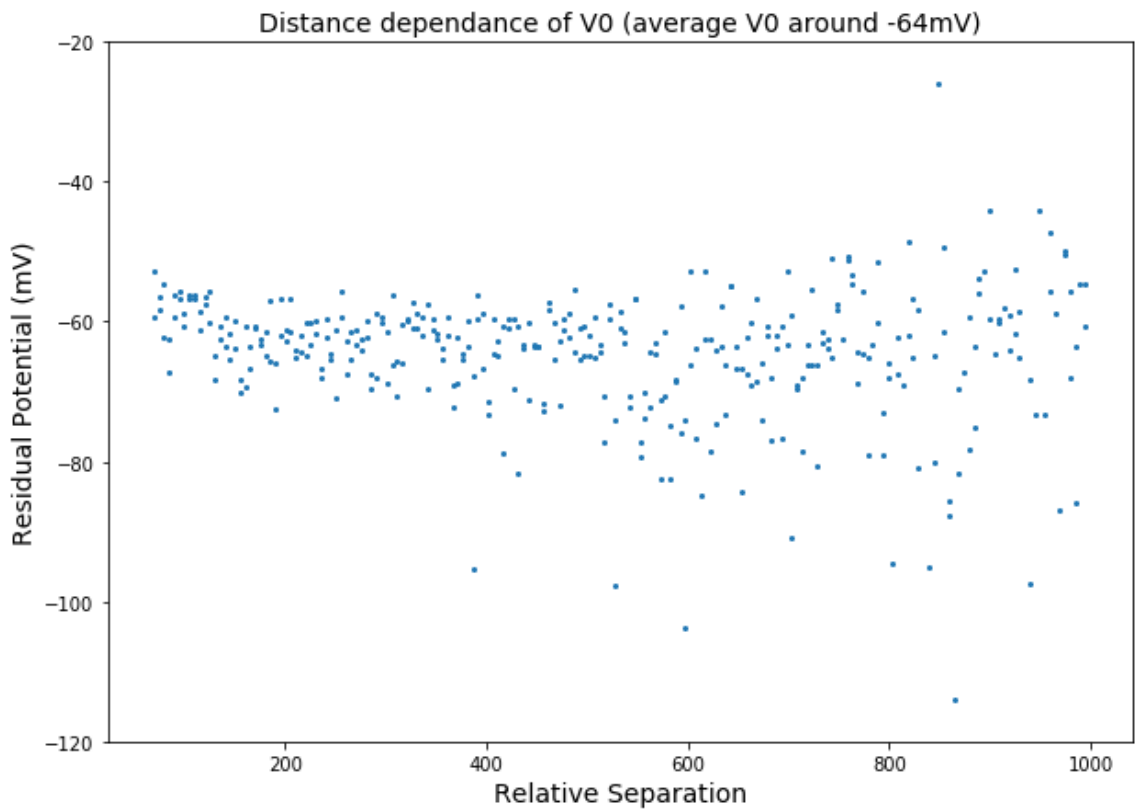
Figure 5.1: The residual potential voltage plotted against the relative separation distance. The right side of the graph corresponds to a flatter part of the frequency shift curve, so it is expected that the fit would be more tenuous. The average residual potential represented here is -61.4±4.1 mV.
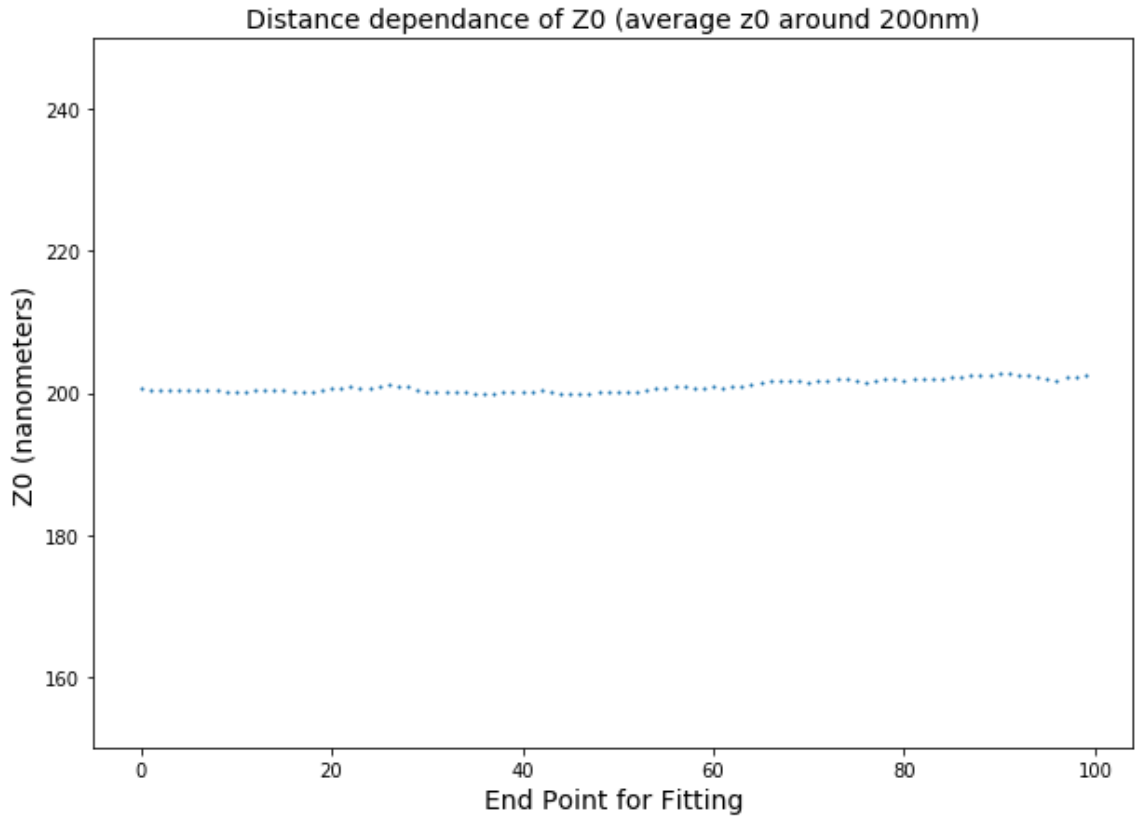
Figure 5.2: The minimum absolute separation, plotted against the relative separation distance included in the fit. Values to the right correspond to fits done with increasingly less of the beta fit curve.

5.2 Minimum Distance

When we fit the curvature of our parabolas to the theory, as discussed in section 4.5, we are able to find a minimum distance of 200.7 nm. We can fit progressively smaller sections of the beta curve to get a sense of the reliability of the fit with less dramatic curves. This is seen in fig. 5.2. The deviation of the z' as we vary the size of the fitting range is shown to be $\pm$ 1.12 angstroms.
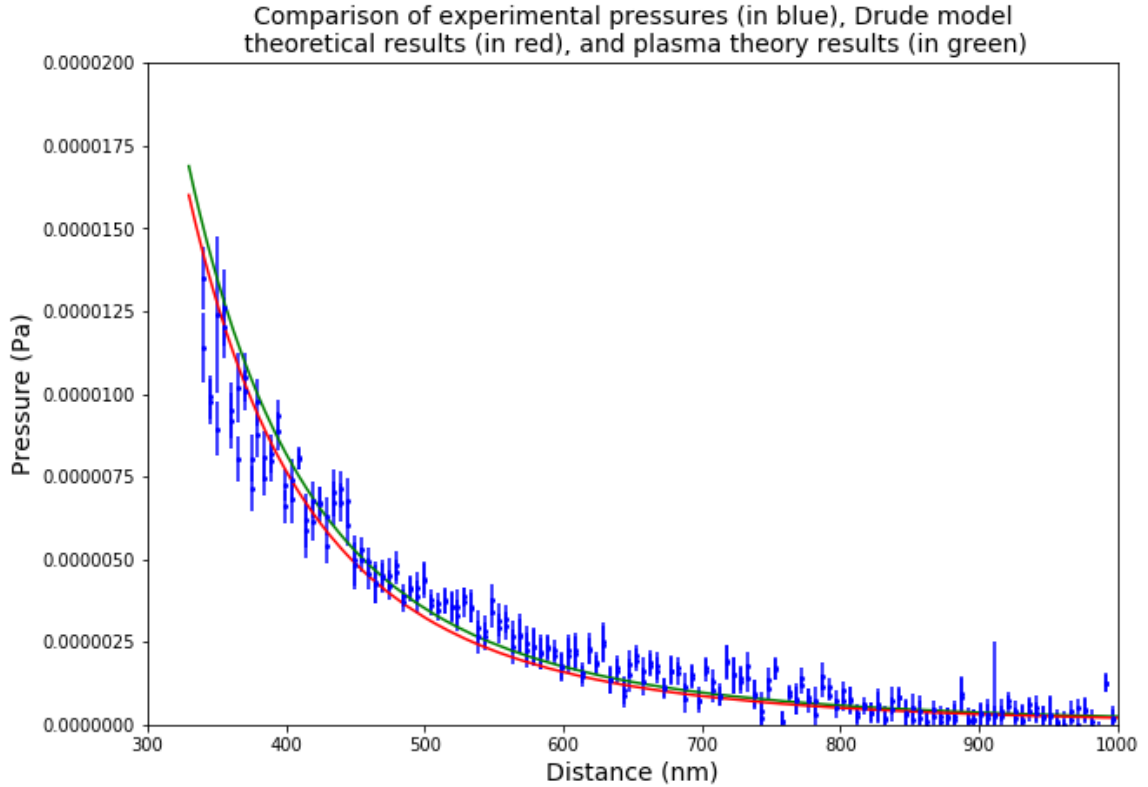
Figure 5.3: A comparison of measured Casimir pressure as a function of separation (in blue) plotted with the calculated Casimir pressure according to the plasma theory of zero-point photon dissipation (in green) and according to the Drude model (in red).

5.3 Comparison with Theory

We plotted the Casimir pressure we calculated from the experimental data against the Casimir pressure calculated according to the PFA modification of the Plasma and Drude model theories. The results are seen in fig. 5.3. The error bars include the systematic error as well as the random error. The results show a broad fit to the theory, but the error are too large to differentiate between the models with and without dissipation of zero-point photons.

5.4   Error Analysis and Corrections

We considered two main types of error in this experiment, random and systematic errors. The random error comes from the averaging of multiple sets into one data point. The formula for random error is given by

$$\delta P_{ran} = \frac{\sigma}{\sqrt{N}}, \tag{5.1}$$

where σ is the standard deviation of the series of measurements, and N is the total number of measurements being averages. We averaged 42 measurements for our result.

The systematic error is chiefly due to the fitting algorithm for the beta curve fit and its application to eq. 4.13. The error from this source can be given by

$$\frac{\delta P_{sys}(z)}{P(z)} = \sqrt{\left(\frac{\delta C}{C}\right)^2 + \left(\frac{\delta f(z)}{f(z)}\right)^2}. \tag{5.2}$$

Our C value was 57413±280, averaged between our runs. The δf value was measured by looking at the frequency noise coming out of the PLL when a frequency generator was used as a minimal noise input to the PLL. The value for δf was 5 mHz.

5.4.1   Roughness Correction

In order to take into account the effect of a surface that is not perfectly flat, we need to take into account a roughness correction to the theory. The correction factor, given by [34], is

$$\eta_R = 1 + 10\frac{\delta_s^2 + \delta_c^2}{z^2} + 105\frac{(\delta_s^2 + \delta_c^2)^2}{z^4} + higher\ order\ terms, \tag{5.3}$$

where δ_s and δ_c are the root-mean-squared roughness of the sphere and cylinder respectively, measured by an atomic force microscope. Our values for δ_s and δ_c were 5.52 nm and 1.05
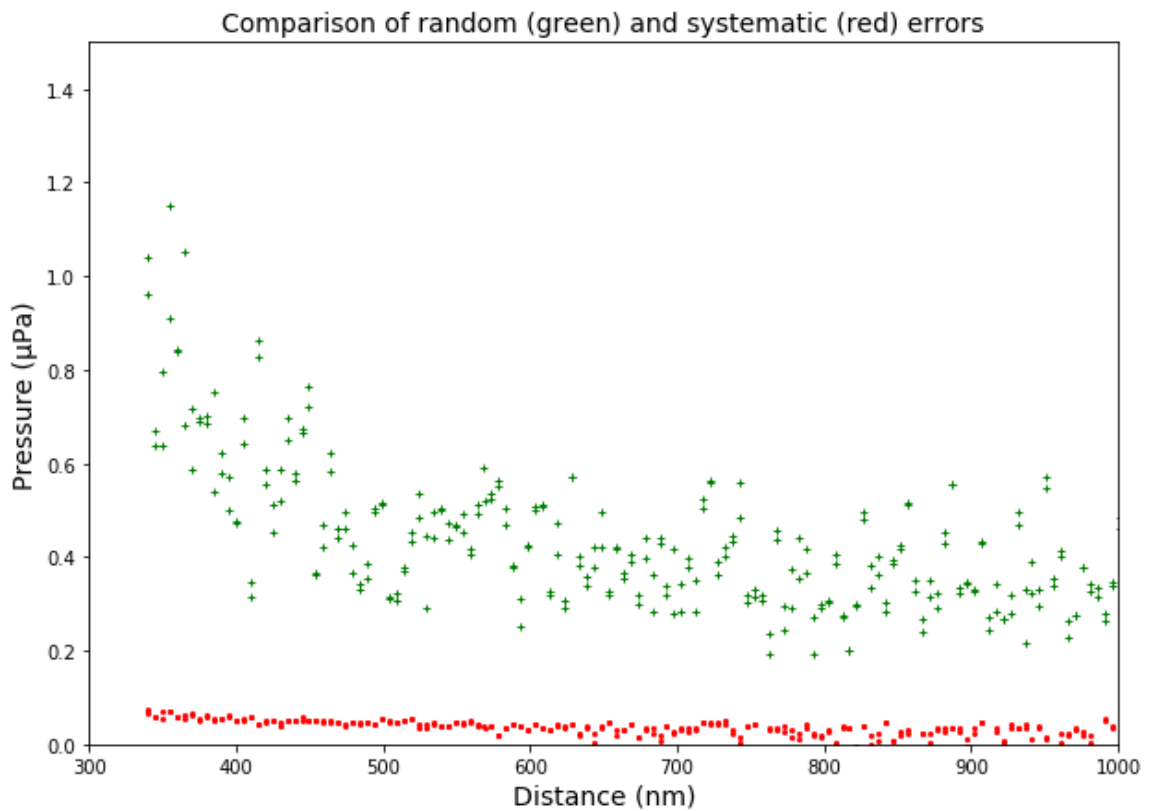
Figure 5.4: A plot of the random and systematic errors as a function of distance. The random error is dominant. The increase in random error at short separation distances corresponds to the increase in noise we saw in the frequency shift data at short separation distances.

Figure 5.5: This graph shows the experimental error in our data when compared with the dissipationless model theoretical predictions. The values here were calculated using $Exp.\ Error = |data - theory|/theory$. The increase in experimental errors at large distances is largely due to a decrease in the theory value.

nm. The additional roughness on the sphere did not have a clear source. The correction to the Casimir pressure at the closest separation distance was about .35%.

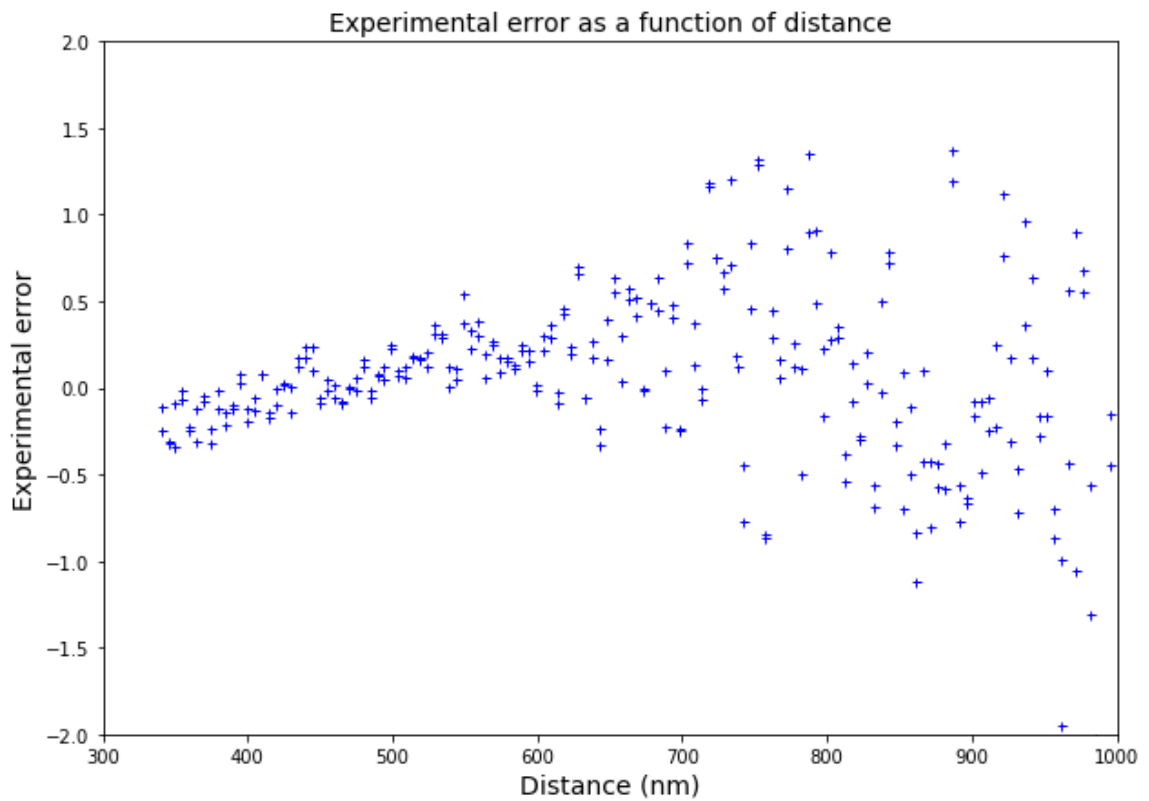The Casimir pressure, with the PFA and roughness corrections applied, is given by

$$F'_{Cas} = 2\pi \bar{R} P_{Cas,pp} * \eta_R.$$ (5.4)

This correction is applied in figure 5.3.

5.4.2 Proximity Force Approximation Corrections

The curvature corrections in the PFA go as

$$1 + \beta \frac{z}{\bar{R}} + \mathcal{O}\left(\frac{z^2}{\bar{R}^2}\right),$$ (5.5)

For the separations and radii we have measured, $z/\bar{R} < 3\%$. This demonstrates the validity of using the PFA at the length scales we are currently measuring. For future studies with smaller radii, or larger separation distances, another approach is necessary, as the curvature corrections to the PFA become large.

Chapter 6

Conclusions

6.1   Conclusion

We were able to measure the Casimir pressure between a sphere and a cylinder, and it showed broad similarity to the PFA Casimir theory between a sphere and a cylinder. The error bars on our data are currently too large to distinguish the difference between the dissipationless and dissipation-included approaches to the Lifshitz theory. The majority of the error arose from the random error, so more measurements would serve to decrease this.

6.2   Future Work

The first step to take in reducing the noise in our system is to increase the amount of data. The data presented here represents only a few successful runs. Taking more data should be effective in reducing the random error in our results.

Another avenue is using a PID loop to control and correct for the drift rate in the separation between the sphere and cylinder. This would require some non-insignificant changes to the experimental set-up, but would allow the acquisition of arbitrary amounts of data at a given separation. The increased sensitivity would allow study of the Casimir effect at large distances.

To further approach the limit of a one dimensional object, the size of the cylinder should be reduced. With cylinders much smaller than the one we used, the corrections to the proximity force approximation would grow overly large. This would necessitate a move towards a multiple scattering approach for the theoretical calculations.

When the sensitivity is improved, further experiments could be performed to further probe the effects of the surface dimensionality on the Casimir effect, through probing the force between two cylinders, with varying angles between their axes.

Bibliography

[1] Hendrick BG Casimir. On the attraction between two perfectly conducting plates. *Front. Phys.*, 100:61–63, 1948.

[2] F London. Z phys chem b 1930, 11, 222; eisenschitz, r.; london, f. *Z Phys*, 60:491, 1930.

[3] Hendrik BG Casimir and Dirk Polder. The influence of retardation on the london-van der waals forces. *Physical Review*, 73(4):360, 1948.

[4] EM Lifshitz. The theory of molecular attractive forces between solids. soo. *Phys. JETP, 2 (1956) 73*, 83, 1956.

[5] Jeremy N Munday, Federico Capasso, and V Adrian Parsegian. Measured long-range repulsive casimir–lifshitz forces. *Nature*, 457(7226):170–173, 2009.

[6] Michael Krech. *The Casimir effect in critical systems*. World Scientific, 1994.

[7] RS Decca, D López, E Fischbach, GL Klimchitskaya, DE Krause, and VM Mostepanenko. Tests of new physics from precise measurements of the casimir pressure between two gold-coated plates. *Physical Review D*, 75(7):077101, 2007.

[8] Umar Mohideen and Anushree Roy. Precision measurement of the casimir force from 0.1 to 0.9 μ m. *Physical Review Letters*, 81(21):4549, 1998.

[9] ME Bowers and CR Hagen. Casimir energy of a spherical shell. *Physical Review D*, 59(2):025007, 1998.

[10] Michael Levin, Alexander P McCauley, Alejandro W Rodriguez, MT Homer Reid, and Steven G Johnson. Casimir repulsion between metallic objects in vacuum. *Physical review letters*, 105(9):090403, 2010.

[11] Alejandro W Rodriguez, Federico Capasso, and Steven G Johnson. The casimir effect in microstructured geometries. *Nature photonics*, 5(4):211, 2011.

[12] Julian Schwinger, Lester L DeRaad Jr, and Kimball A Milton. Casimir effect in dielectrics. *Annals of Physics*, 115(1):1–23, 1978.

[13] R Castillo-Garza, J Xu, GL Klimchitskaya, VM Mostepanenko, and U Mohideen. Casimir interaction at liquid nitrogen temperature: Comparison between experiment and theory. *Physical Review B*, 88(7):075402, 2013.

[14] CI Sukenik, MG Boshier, and D Cho. V. sandoghar, and ea hinds. *Phys. Rev. Lett*, 70(5), 1993.

[15] F De Martini, G Innocenti, GR Jacobovitz, and P Mataloni. Anomalous spontaneous emission time in a microscopic optical cavity. *Physical review letters*, 59(26):2955, 1987.

[16] Leandros Perivolaropoulos. Vacuum energy, the cosmological constant, and compact extra dimensions: Constraints from casimir effect experiments. *Physical Review D*, 77(10):107301, 2008.

[17] Emilio Elizalde. Uses of zeta regularization in qft with boundary conditions: a cosmo-topological casimir effect. *Journal of Physics A: Mathematical and General*, 39(21):6299, 2006.

[18] VA Kuzmin, II Tkachev, and ME Shaposhnikov. Restrictions imposed on light scalar particles by measurements of van der waals forces. *JETP Letters*, 36(2):59–62, 1982.

[19] Joshua C Long, Hilton W Chan, Allison B Churnside, Eric A Gulbis, Michael CM Varney, and John C Price. Upper limits to submillimetre-range forces from extra space-time dimensions. *Nature*, 421(6926):922–925, 2003.

[20] VM Mostepanenko and I Yu Sokolov. The casimir effect leads to new restrictions on long-range force constants. *Physics Letters A*, 125(8):405–408, 1987.

[21] VM Mostepanenko and I Yu Sokolov. Restrictions on long-range forces following from the casimir effect. *Soviet Journal of Nuclear Physics*, 46(4):685–688, 1987.

[22] RS Decca, D López, E Fischbach, GL Klimchitskaya, DE Krause, and VM Mostepanenko. Novel constraints on light elementary particles and extra-dimensional physics from the casimir effect. *The European Physical Journal C*, 51(4):963–975, 2007.

[23] Sung Min Kim, Emil B Song, Sejoon Lee, Sunae Seo, David H Seo, Yongha Hwang, R Candler, and Kang L Wang. Suspended few-layer graphene beam electromechanical switch with abrupt on-off characteristics and minimal leakage current. *Applied Physics Letters*, 99(2):023103, 2011.

[24] W-H Lin and Y-P Zhao. Casimir effect on the pull-in parameters of nanometer switches. *Microsystem Technologies*, 11(2-3):80–85, 2005.

[25] F Michael Serry, Dirk Walliser, and G Jordan Maclay. The role of the casimir effect in the static deflection and stiction of membrane strips in microelectromechanical systems (mems). *Journal of Applied Physics*, 84(5):2501–2506, 1998.

[26] Y-P Zhao, LS Wang, and TX Yu. Mechanics of adhesion in mems—a review. *Journal of Adhesion Science and Technology*, 17(4):519–546, 2003.

[27] F Chen, GL Klimchitskaya, VM Mostepanenko, and U Mohideen. Control of the casimir force by the modification of dielectric properties with light. *Physical review B*, 76(3):035338, 2007.

[28] C-C Chang, AA Banishev, GL Klimchitskaya, VM Mostepanenko, and U Mohideen. Reduction of the casimir force from indium tin oxide film by uv treatment. *Physical review letters*, 107(9):090403, 2011.

[29] Philippe Andreucci, Laurent Duraffourg, Eric Ollier, Valerie Nguyen, Marie Therese Delay, and Philippe Robert. Impact of casimir force on nano accelerometers modeling. In *SENSORS, 2006 IEEE*, pages 1057–1060. IEEE, 2006.

[30] Li Shen, Shi Qiao Gao, and Yan Wei Guan. The effect of casimir force to the performance of the micro-accelerometer. In *Key Engineering Materials*, volume 562, pages 247–250. Trans Tech Publ, 2013.

[31] Marcus J Sparnaay. Measurements of attractive forces between flat plates. *Physica*, 24(6-10):751–764, 1958.

[32] Peter HGM van Blokland and J Theodoor G Overbeek. van der waals forces between objects covered with a chromium layer. *Journal of the Chemical Society, Faraday Transactions 1: Physical Chemistry in Condensed Phases*, 74:2637–2651, 1978.

[33] Steven K Lamoreaux. Demonstration of the casimir force in the 0.6 to 6 μ m range. *Physical Review Letters*, 78(1):5–8, 1997.

[34] C-C Chang, AA Banishev, R Castillo-Garza, GL Klimchitskaya, VM Mostepanenko, and U Mohideen. Gradient of the casimir force between au surfaces of a sphere and a plate measured using an atomic force microscope in a frequency-shift technique. *Physical Review B*, 85(16):165443, 2012.

[35] Giacomo Bressi, Giovanni Carugno, Roberto Onofrio, and Giuseppe Ruoso. Measurement of the casimir force between parallel metallic surfaces. *Physical review letters*, 88(4):041804, 2002.

[36] Alexander Stange, Matthias Imboden, Josh Javor, Lawrence K Barrett, and David J Bishop. Building a casimir metrology platform with a commercial mems sensor. *Microsystems & nanoengineering*, 5(1):1–9, 2019.

[37] Hugo C Hamaker. The london—van der waals attraction between spherical particles. *physica*, 4(10):1058–1072, 1937.

[38] V Adrian Parsegian. *Van der Waals forces: a handbook for biologists, chemists, engineers, and physicists*. Cambridge University Press, 2005.

[39] Michael Bordag, Umar Mohideen, and Vladimir M Mostepanenko. New developments in the casimir effect. *Physics reports*, 353(1-3):1–205, 2001.

[40] Paul Drude. On the electron theory of metals. *Annals of physics*, 306(3):566–613, 1900.

[41] Valdir Barbosa Bezerra, GL Klimchitskaya, and VM Mostepanenko. Higher-order conductivity corrections to the casimir force. *Physical Review A*, 62(1):014102, 2000.

[42] VB Bezerra, GL Klimchitskaya, and VM Mostepanenko. Thermodynamical aspects of the casimir force between real metals at nonzero temperature. *Physical Review A*, 65(5):052113, 2002.

[43] VB Bezerra, GL Klimchitskaya, VM Mostepanenko, and C Romero. Violation of the nernst heat theorem in the theory of the thermal casimir force between drude metals. *Physical Review A*, 69(2):022119, 2004.

[44] J Błocki, J Randrup, WJ Światecki, and CF Tsang. Proximity forces. *Annals of Physics*, 105(2):427–462, 1977.

[45] VA Kirsch. Calculation of the van der waals force between a spherical particle and an infinite cylinder. *Advances in Colloid and Interface Science*, 104(1-3):311–324, 2003.

[46] CC Speake and C Trenkel. Forces between conducting surfaces due to spatial variations of surface potential. *Physical review letters*, 90(16):160403, 2003.

[47] Woo-Joong Kim, AO Sushkov, Diego AR Dalvit, and SK Lamoreaux. Surface contact potential patches and casimir force measurements. *Physical Review A*, 81(2):022505, 2010.

[48] RO Behunin, Y Zeng, DAR Dalvit, and S Reynaud. Electrostatic patch effects in casimir-force experiments performed in the sphere-plane geometry. *Physical Review A*, 86(5):052509, 2012.

[49] RO Behunin, F Intravaia, DAR Dalvit, PA Maia Neto, and S Reynaud. Modeling electrostatic patch effects in casimir force measurements. *Physical Review A*, 85(1):012504, 2012.

[50] David R Lide. *CRC handbook of chemistry and physics*, volume 85. CRC press, 2004.

[51] Robert Schafer, Jun Xu, and Umar Mohideen. In situ ion gun cleaning of surface adsorbates and its effect on electrostatic forces. *International Journal of Modern Physics A*, 31(02n03):1641025, 2016.

[52] John R Vig. Uv/ozone cleaning of surfaces. *Journal of Vacuum Science & Technology A: Vacuum, Surfaces, and Films*, 3(3):1027–1034, 1985.

[53] NS McIntyre, RD Davidson, TL Walzak, R Williston, M Westcott, and A Pekarsky. Uses of ultraviolet/ozone for hydrocarbon removal: Applications to surfaces of complex composition or geometry. *Journal of Vacuum Science & Technology A: Vacuum, Surfaces, and Films*, 9(3):1355–1359, 1991.

[54] Jun Xu, GL Klimchitskaya, VM Mostepanenko, and U Mohideen. Reducing detrimental electrostatic effects in casimir-force measurements and casimir-force-based microdevices. *Physical Review A*, 97(3):032501, 2018.

[55] Ehsan Noruzifar, Thorsten Emig, Umar Mohideen, and Roya Zandi. Collective charge fluctuations and casimir interactions for quasi-one-dimensional metals. *Physical Review B*, 86(11):115449, 2012.

[56] Sahand Jamal Rahi, Thorsten Emig, Noah Graham, Robert L Jaffe, and Mehran Kardar. Scattering theory approach to electrodynamic casimir forces. *Physical Review D*, 80(8):085021, 2009.

[57] DE Krause, RS Decca, D López, and E Fischbach. Experimental investigation of the casimir force beyond the proximity-force approximation. *Physical review letters*, 98(5):050403, 2007.